NUMERICAL MODELING OF THE TRANSITION FROM KINETICS TO DIFFUSION CONTROLLED COMBUSTION OF ALUMINUM PARTICLES

by

Brian T. Bojko
May 7, 2014

A thesis submitted to the
Faculty of the Graduate School of
the University at Buffalo, State University of New York
in partial fulfilment of the requirements for the
degree of

Master of Science

Department of Mechanical & Aerospace Engineering

ProQuest LLC.
789 East Eisenhower Parkway
P.O. Box 1346
Ann Arbor, MI 48106 - 1346

The thesis of Brian T. Bojko was reviewed by the following:

Paul DesJardin
Professor of Mechanical and Aerospace Engineering
Thesis Advisor, Chair of Committee

James Felske
Professor of Mechanical and Aerospace Engineering
Committee Member

Jon Yoo
Assistant Professor of Mechanical and Aerospace Engineering
Committee Member

Acknowledgments

I would like to thank my advisor, Dr. Paul E. DesJardin, for his continuous support, encouragement and guidance throughout during my thesis research. I would also like to thank all of my colleagues for their input and intriguing conversations. Finally, I would like to thank my wife who has always been supportive of all of my goals.

Support for this work has been provided by NAVAIR through the STTR phase II program under contract N68335-10-C-0418.

Table of Contents

List of Tables

List of Figures

Nomenclature

D	mass diffusivity $[m^2/s]$
D_p	particle diameter $[m]$
e_t	total energy $[J/kg]$
H_t	total enthalpy $[J/kg]$
$h^o_{f,i}$	heat of formation of species i $[J/kg]$
h_{vap}	latent heat of vaporization of aluminum $[J/kg]$
K	burn rate constant $[m^2/s]$
$\dot{m}_i$	mass flow rate $[kg/s]$
$\dot{m}'''_i$	mass source term of species i $[kg/m^3s]$
$\dot{m}'''_F$	mass consumption rate of fuel $[kg/m^3s]$
m_o	initial mass of the particle $[kg]$
m_q	mass of quenched particle $[kg]$
$\dot{m}_T$	bulk mass flow rate in radial coordinates $[kg/s]$
r	radial coordinate $[m]$
$\dot{S}$	flow rate of species towards the surface $[kg/s]$
S_L	flame speed $[m/s]$
τ_b	burn time $[s]$
T	temperature $[K]$
Y_i	species mass fraction
Z	mixture fraction

Greek

α	thermal diffusivity $[m^2/s]$
γ	constituent density $[kg/m^3]$
ν	mass based stoichiometric ratio
ρ	mixture density $[kg/m^3]$
ρ_{air}	density of ambient air $[kg/m^3]$
ρ_u	density of unburnt mixture $[kg/m^3]$
φ	constituent volume fraction
Φ	equivalence ratio

subscripts/superscripts

i	i^{th} species
l	liquid property
q	quenching limit
s	particle surface
T	total property
∞	ambient/far-field conditions

Abstract

Aluminum particle burn rates are known to be a strong function of particle size as the mode of burning transitions from diffusion to kinetically controlled. To better understand the rate dependent diffusion and kinetic processes, a fully compressible, one-dimensional, axisymmetric particle burn model is developed. Several cases are conducted to explore the burning of aluminum particles in air, carbon-dioxide and steam environments. Predictions of burn rates versus particle size reveal significant deviations from a diffusion controlled burning limit, highlighting the importance of accounting for finite-rate chemistry in modeling the burning of submicron aluminum particles. While overall agreement to data is satisfactory, the detailed model cannot be directly used in system level tools due to computational cost. Two reduced modeling strategies are therefore explored to account for finite-rate chemistry effects in simpler models for use in system level CFD analysis. The first is an augmented $D^2 - law$ where the finite-rate chemistry is treated as a perturbation to flame sheet approximation *via* augmented burn rate "constants". Predictions using this approach of deflagration speeds in dusty aluminum-air gases agree well with experiments and show evidence of a maximum flame speed for a given mass loading. The second modeling approach uses a reduced numerical model and kinetics mechanism resulting in computationally efficient solutions. Results using this approach show up to two orders of magnitude reduction in computational effort while maintaining reasonable accuracy for predictions of flame structure, burn rates and burn times.

Chapter 1

Modeling the Transition from Diffusion to Kinetically Controlled Combustion

1.1 Introduction

The use of aluminum particles continues to be of interest as an additive for propellants [10] and aviation fuels [11, 12] to increase energy density and specific impulse. Recent studies have focused on the transition of diffusion to kinetically controlled burning with decreasing particle size [13, 4, 14]. One of the motivations for studying this transition is the potential of using submicron to nano-scale sized particles in fuels to shorten ignition times [15] and accelerate flame speeds [4].

The transition of diffusion to kinetically controlled combustion was studied by Bazyn *et al.* and Lynch *et al.* as a function of both particle size and pressure using a reflected shock-tube facility for O_2 and CO_2 environments [13, 16]. For a pressure of $8.5\,atm$, the limit of a diffusion flame was observed to occur for particle sizes less than ~ 20 microns as reactions migrate closer to the droplet surface.

Aluminum particle combustion in the $2 - 20$ micron range was studied by Badiola *et al.* by igniting particles generated using an electro-static aerosol generator and ignited with a CO_2 laser [17]. Using AlO emission measurements to determine burn times and average temperatures, Badiola *et al.* estimated the transition from diffusion to kinetically controlled combustion at ~ 10 microns in air.

Washburn *et al.* conducted detailed numerical simulations of aluminum particles in oxygen,

carbon dioxide and steam environments [14, 18]. Cases were conducted using $3-11$ micron sized particles and compared to burn time data from Bazyn *et al.*[13, 19]. Overall agreement was reasonable with some discrepancies observed for pressures below $\sim 10\ atm$ in CO_2 and H_2O environments. Differences were attributed to the distribution of particles in the experiments which tends to skew burn time measurements at lower pressures.

Huang *et al.* conducted a study of flame speed of aluminum particle dust in air [4]. Model predictions of flame speed are compared to data using phenomenologically derived burn rate models. For larger micron-sized particles, ignition temperature is correlated with data and the overall mixture burn rate uses particle burn time correlations developed by Beckstead [20]. For smaller nano-sized particles, the burn rates are assumed to follow that of a molecular limit using the chemical kinetics mechanism developed by Catoire *et al.* [21]. Flame speed predictions are shown to scale with decreasing particle diameter as $\sim d^{-0.92}$, consistent with D^2 theory (see discussion regarding estimates of S_L in results section). For particles less than ~ 10 microns, however, further reduction in particle diameter results in a more gradual increase in flame speed, scaling as $\sim d^{-0.52}$, as the rate of burning becomes more kinetically controlled. Huang *et al.* estimate a maximum flame speed of $5.82\,m/s$ as the particle diameter reaches a molecular asymptotic limit.

The transition from diffusion to kinetically controlled combustion is a recurring theme in the aforementioned studies and plays a crucial role in burning modes for decreasing pressures and particle sizes. In particular, particles that are ~ 10 microns and smaller exhibit a clear dependence on the rate limiting chemical kinetics. Relations between the Damköhler and Knudsen numbers have been made to help describe the mode of combustion of particles [22], but to date there have not been theoretical estimates of this transition as a function of particle size for aluminum particles, although estimates have been made for other energetic materials [23, 24]. Typically, considerations of such a transition have been studied through the correlation of burn times versus pressure which exhibits a transition when pressure decreases and burn times increase. If pressure is held constant, burn rates will be a function of particle diameter and asymptotically approach a converged, diffusion-controlled burn rate as particle size increases.

While experimentally derived empirical burn time relations have been developed to account for the burning behavior of aluminum particles for different burning regimes [25, 16, 26, 17], they are limited to the select conditions of the experiment where the far-field temperature, pressure and oxidizer are held constant during the burning process. In system level applications using aluminum particulate (*e.g.*, a rocket motor) the far-field conditions will most likely not remain constant. While detailed CFD models such as those by Washburn *et al.* [14, 18] and Gallier *et al.* [27] do account for varying far-field conditions, they are far too complex for use with system level simulations of multiphase flows involving billions of particles. An alternative description is therefore desirable which can balance complexity with accuracy of burn rates as the particle transitions from diffusion to kinetically controlled limits. Exploring modeling strategies which can accommodate these constraints is a focus of this study.

The rest of the study is as follows. A fully compressible, one-dimensional, axisymmetric

model formulation is first presented that accounts for the full chemistry, differential diffusion, *etc.* using kinetic theory of gases. The purpose of the detailed model is to serve as the "exact" solution for which reduced approaches can be compared against. Validation is conducted using the experimental data and simulations of Bucher *et al.* [3] and measurements of Bazyn *et al.* [13] and also to numerical simulations of Washburn *et al.* [14] which span the diffusion to kinetically controlled burning transition regime. Two reduced modeling approaches are explored. The first relies on couching burn rates in terms of a modified D^2-law where a normalized burn rate "constant" (K) becomes a function of particle diameter and pressure to account for the effects of finite-rate chemistry. The normalized burn rate constants can be combined with eigenvalue based analytical solutions of the flame structure to account for effects of finite-rate chemistry. This model is is used to compute flame deflagration speeds of dusty aluminum-air gases and compared to theory and data. The second reduced model is a simplified numerical model that employes quasi-steady assumption of mass transfer and reduced kinetics allowing for an efficient fully implicit formulation. Flame structure comparisons are presented using this model compared to the more general fully compressible formulation and errors in burn rates and flame structure are characterized.

Chapter 2

Model Formulation

The starting point for a detailed model is a spherically symmetric particle. Since the focus of this study is not to explore multi-dimensional effects, a spherically symmetric configuration is the simplest geometry that needs to be considered for studying diffusion to kinetically controlled burning. The multiphase gas flow is considered one-dimensional, fully compressible and viscous resulting in the following set of transport equations for mass, species, momentum and energy conservation.

$$\frac{\partial(\rho r^2)}{\partial t} + \frac{\partial(\rho u r^2)}{\partial r} = 0 \tag{2.1a}$$

$$\frac{\partial(\rho Y_i r^2)}{\partial t} + \frac{\partial(\rho u Y_i r^2)}{\partial r} = \frac{\partial}{\partial r}\left(r^2 \rho D_i \frac{\partial Y_i}{\partial r}\right) + \dot{m}_i''' r^2 \tag{2.1b}$$

$$\frac{\partial(\rho u r^2)}{\partial t} + \frac{\partial(\rho u^2 r^2)}{\partial r} = -r^2 \frac{\partial p}{\partial r} + \frac{\partial}{\partial r}\left[r^2 \mu \left(2\frac{\partial u}{\partial r} - \frac{2}{3}\left(\frac{\partial u}{\partial r} + u/r\right)\right)\right] \tag{2.1c}$$

$$\begin{aligned}\frac{\partial(\rho e_t r^2)}{\partial t} + \frac{\partial(\rho u H_t r^2)}{\partial r} &= \frac{\partial}{\partial r}\left[r^2 u \mu \left(2\frac{\partial u}{\partial r} - \frac{2}{3}\left(\frac{\partial u}{\partial r} + u/r\right)\right)\right] \\ &+ \frac{\partial}{\partial r}\left[r^2\left(k\frac{\partial T}{\partial r} + \sum_i^N \rho D_i \frac{\partial Y_i}{\partial r} h_i\right)\right] - r^2 \sum_i^N \dot{m}_i''' h_{f,i}^o\end{aligned} \tag{2.1d}$$

where $e_t (= e + u_r^2/2)$ is the total sensible energy, $H_t (= e_t + p/\rho)$ is the total enthalpy and u is the radial component of velocity. CHEMKIN formatted reaction mechanisms and transport properties (*i.e.* C_P, k, D_{i-j}, *etc.*), are tabulated for each temperature and pressure between 300 K and 5000 K; and 0.5 atm and 30 atm for efficient lookup during run-time. Mixing rules of Mathur *et al.* [28] and Bird *et al.* [29] are used to determine mixture weighted diffusion (D_i) and thermal conductivity (k), respectively. Soret and Dufor diffusion effects are neglected. A locally homogenous flow (LHF) approximation is employed to account for the alumina condensate where the diffusion coefficient of alumina is set to be the lowest of the gas-phase constituents, consistent with previous studies [27]. The density in Eq. (2.1) represents the mixture density of solid and gas phases, $\rho = \gamma_s \varphi_s + \gamma_g \varphi_g$, where γ and φ are the density and volume fraction for each phase.

The density of solid phase alumina is assumed to be a constant, $\gamma_s = 3950\,kg/m^3$. Consistent with the LHF approximation, pressure and thermal equilibrium is assumed to exist between the solid and gas phases.

The aluminum oxidization mechanism used by Washburn [30, 14] is employed in this study and summarized in B.1. This mechanism consists of 46 reaction steps and 22 species for oxidation in O_2, CO_2 and H_2O environments. Although new reaction pathways have recently been considered for aluminum-steam environments by Starik *et al.* [31], they have not been included in the current mechanism. It is assumed that condensation reactions occur in the gaseous phase and migrate to the surface of the particle to produce the alumina cap. The deposition of alumina is assumed sufficiently fast such that alumina at the surface is zero. This assumption provides an upper limit on the amount of alumina that can be deposited to the surface and has shown to provide reliable estimates of deposition rates in previous studies [32]. Other mechanisms have been postulated for the deposition of alumina onto the particle surface, such as the entrainment of metal oxide particles into a recirculation zone on the leeward side of the particle [33]. Such mechanisms are not considered in the present study. All other species are assumed insoluble in the liquid aluminum and therefore mass fluxes are set equal to zero at the surface. The heat transfer into the liquid is neglected, employing an isothermal assumption. The resulting boundary conditions are as follows,

$$\text{mass:} \qquad \dot{m}_T = \dot{m}_{Al} - \dot{S}_{Al_2O_3} \tag{2.2a}$$

$$\text{aluminum:} \qquad \dot{m}_{Al,l} = \dot{m}_T Y_{Al_s} - 4\pi r_s^2 \rho D_{Al} \left.\frac{dY_{Al}}{dr}\right|_s \tag{2.2b}$$

$$\text{alumina:} \qquad -\dot{S}_{Al_2O_3} = -4\pi r_s^2 \rho D_{Al_2O_3} \left.\frac{dY_{Al_2O_3}}{dr}\right|_s \tag{2.2c}$$

$$\text{other species:} \qquad 0 = \dot{m}_T Y_{i,s} - 4\pi r_s^2 \rho D_i \left.\frac{dY_i}{dr}\right|_s \tag{2.2d}$$

$$\text{energy:} \qquad \dot{m}_{Al,l} h_{vap} = 4\pi r_s^2 k_g \left.\frac{dT}{dr}\right|_s \tag{2.2e}$$

where $\dot{S}_{Al_2O_3}$ is the rate of alumina deposition to the particle surface. Assuming saturation conditions at the liquid-vapor interface, the partial pressure of the aluminum vapor is related to the surface temperature (T_s) using a vapor pressure curve from Washburn *et al.* $p_{Al} = exp\left[36.547 - 39033/T_s - 1.3981\ ln(T_s) + 6.7839 \times 10^{-9}\ T_s^2\right]$ [34].

A finite volume method is used to solve the coupled system of non-linear equations given in Eq. (2.1) using the surface boundary condition of Eq. (A.2) and defining the far-field conditions for all species, temperature and pressure. A second-order fractional step method is used to integrate the equations using a two-stage Runge-Kutta (RK) time integration. In this approach, source terms are constructed for processes of convection, diffusions and reactions. Convective fluxes are discretized using an AUSM+UP flux vector splitting [35] using a combination of second-order upwind biased and essentially non-oscillatory (ENO) interpolants for determin-

ing fluxes [36, 37]. Molecular fluxes are approximated using second-order centered differencing employing a semi-implicit operator to avoid diffusion time step stability limitations. Chemical reactions are advanced for each RK stage using a semi-implicit RK solver with adaptive time step control. The equations are marched in time until a steady-state solution is achieved for determining burning rates and flame structure.

A critical aspect of the burning process of aluminum is the condensation and volatilization of the alumina. This phase change is primarily responsible for the increase in thermal energy when the condensate is formed. Liang and Beckstead developed a two-stage alumina condensation model using homogeneous nucleation theory along with an empirical set of constants which are tuned using experimental data [20]. A simpler approach is pursued here where the aluminum oxide is assumed to be in local phase-equilibrium with the surroundings. To determine the equilibrium concentrations, thermodynamic properties of gaseous Al_2O_3 are used from Swihart and Catoire [38] based on their *ab initio* molecular orbital calculations. Figure 2.1a shows representative predictions of Al, O_2, AlO, Al_2O, Al_2O_3, O and mixture temperature using this approach as a function of mixture enthalpy. These results are in good agreement with the estimates of Glassman shown in Fig. 2.1b and experimental work done by Lynch *et al.* [39] on the volatilization temperature of alumina and supports the concept of a limiting temperature associated with the dissociation of Al_2O_3 condensate.

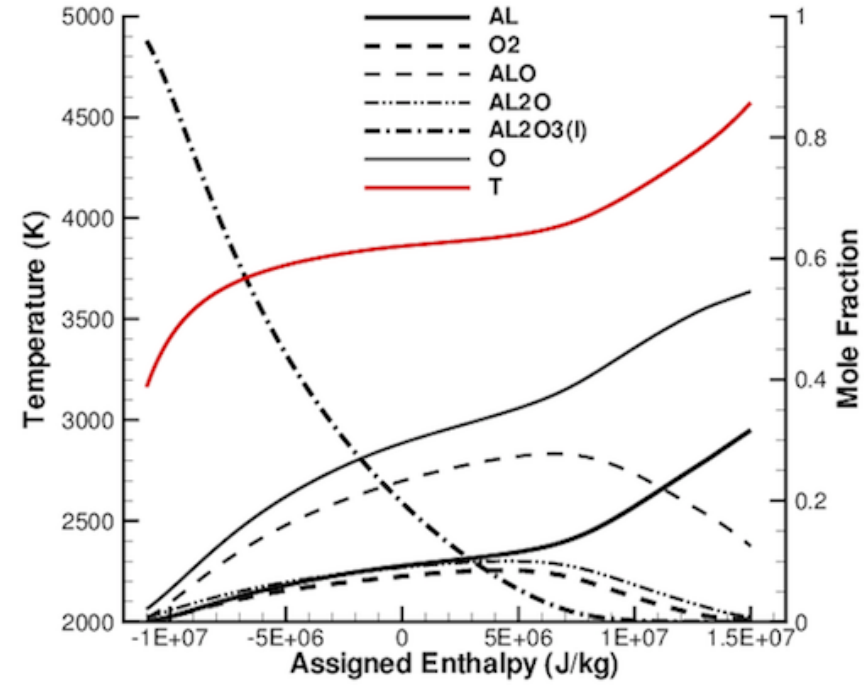

(a)

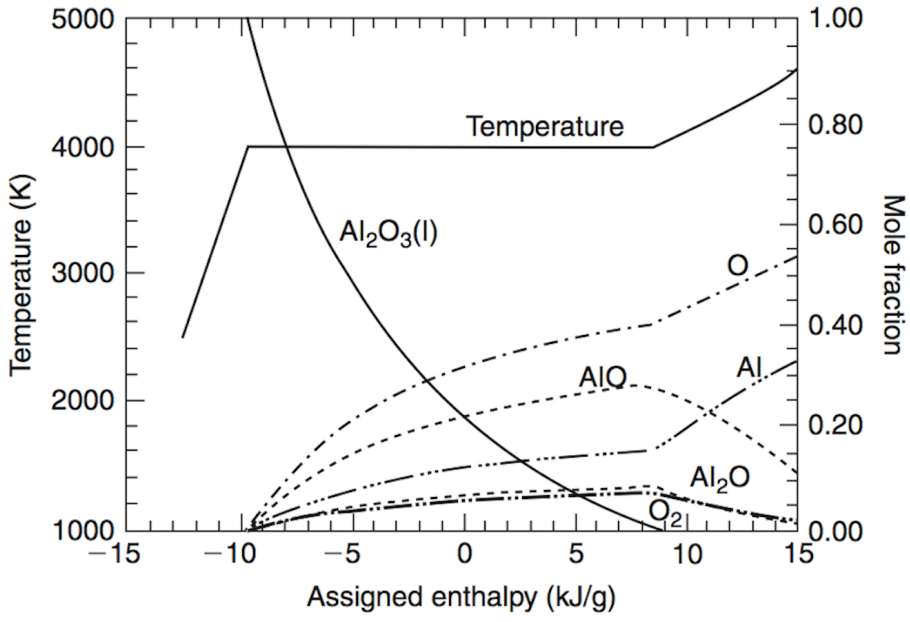

(b)

Figure 2.1. Stoichiometric equilibrium calculations of current mechanism (a) as compared to equilibrium calculations considering the dissociation of alumina by Glassman [1] (b)

Chapter 3

Results and Discussion

To validate the detailed model, $220\mu m$ particle diameter cases are first conducted and compared to flame structure measurements of Bucher *et al.* [2]. To the author's knowledge, the data of Bucher *et al.* continues to serve as the sole source of flame structure data for aluminum combustion and is an excellent resource for model validation. Figure 3.1 shows comparisons of normalized mass fractions of AlO and Al_2O_3 along with temperature. Overall agreement to data is excellent with comparisons of AlO, matching the data within 10% error. The peak mass fraction of Al_2O_3 and the predicted profile also agrees well with the data. Remaining differences may be due in part to differences in chemical mechanism and diffusion models used for the alumina condensate.

Decreasing particle size results in a lower flame temperature and a migration of the flame to the surface. During this transition, the overall rate of burning transitions from a diffusion to kinetically controlled process. This may be readily shown theoretically by considering the limit of steady burning and mapping the species conservation equation in terms of mixture fraction, Z (assuming constant diffusivity, D, for all species). In this limit, the overall mass flow rate ($\dot{m} = 4\pi\rho u r^2$) is constant, therefore Eq. (2.1b) becomes $d^2Y_i/dZ^2 = 2\dot{m}_i'''/(\rho\chi)$ where χ is the scalar dissipation rate. Solving the mixture fraction equation in spherical coordinates, χ may be derived analytically, $\chi \equiv 2D[(\dot{m}\ Z - \dot{m}_Z)/(4\pi\rho D r^2)]^2$. In this expression, $\dot{m}_Z$ is the overall flow rate of mixture fraction and is a constant for steady burning. Near the flame at $Z = Z_{st}$, χ_{st} is proportional to $1/r^4$, indicating the fuel loading into the flame is a strong function of particle size. As the particle radius decreases, χ rapidly increases, reducing the effective chemical reaction rates. A reduction in the conversion rates results in the transition of burning from diffusion to kinetics controlled. From this analysis, it is reasonable to assume that all burning droplets will transition from diffusion to kinetically controlled modes of burning. The importance of the kinetically controlled burning regime of a droplet is therefore a function of what fraction of the total burning time is dominated by kinetic effects. For aluminum particles, the transitional size appears to be approximately $10\mu m$ but is also strongly dependent on pressure through its

effect on the diffusion coefficient. Further information on the derivation and discussion on the mixture fraction formulation can be found in Appendix A.

To explore the transitional burning regime of aluminum particles, the experimental data of Bazyn *et al.* [13] [19] , Lynch *et al.* [16], and detailed numerical simulations of Washburn *et al.* [30, 14] are used for comparison purposes. The experiments report burn times of aluminum in Ar-oxidizer mixtures with varying pressures where burn times are estimated using light emission collected from photo-diodes. For this comparison, burn times are computed as,

$$\tau_b = \int_{m_q}^{m_o} \frac{dm}{\dot{m}_{Al}} \tag{3.1}$$

where m_o and m_q are the initial and quenched masses, respectively. m_q is determined by systematically reducing the initial mass until a meaningful steady burning solution can no longer be found. Figures 3.2-3.4 show comparisons of burn times with varying (a) pressure and (b) far-field oxidizer using O_2, CO_2 and H_2O, respectively. Changes in the resulting flame structure are summarized in Figs. 3.5-3.9 showing flame structure at low and high pressures for each oxidizer.

For the O_2 cases in Fig. 3.2, a smooth increase in burn times with decreasing pressure is observed as the mode of burning transitions from diffusion to kinetically controlled, resulting in lower burn rates. Within the uncertainty of the data, good agreement is observed between the detailed model predictions and the data. The detailed model predictions are consistently lower than those from Washburn *et al.* due to differences in the calculation of burn times. In Washburn *et al.*, burn times are computed assuming $m_q = 0$, leading to larger values of τ_b. Changes in the burn rates during this transition can be understood by comparing changes in the flame structure at low pressure (Fig. 3.5) versus high pressure (Fig. 3.6). At high pressure, the flame stand-off is slightly larger and peak flame temperature is 10% higher. The flame temperature and formation of Al_2O_3 is largely controlled by the transport of three species, Al, AlO and Al_2O_3. Distribution of the minor species is shown in Fig. 3.6b for the high pressure case. Al from the surface diffuses to the flame and forms AlO on the fuel rich side of the flame. The AlO formed in the flame diffuses back to the surface forming Al_2O. Al_2O, in turn, diffuses back to the flame, undergoing further oxidation to ultimately form Al_2O_3. The rate of Al_2O_3 formation and peak temperature is therefore limited by the concentration of Al_2O at the particle surface. At high pressures, the mass fraction of Al_2O at the surface is 0.6 (Fig. 3.6b) compared to 0.18 at lower pressures (Fig. 3.5b). A higher concentration results in a higher mass loading of Al_2O into the flame to form Al_2O_3. The concentration of Al_2O at the surface, however, is a function of how quickly AlO is converted to Al_2O near the particle surface. At high pressures all of the AlO is consumed at the particle surface (Fig. 3.6b) therefore the rate of burning is controlled by the diffusion of Al_2O. Decreasing the pressure within the high pressure regime ($P > 10\,atm$) doesn't alter the flame structure much since the concentration of AlO at the flame surface remains zero. At low pressures, however, the mass fraction of AlO starts to grow, reaching 30% of its peak value for the $P = 4\,atm$ case shown in Fig. 3.5b. Subsequently, Al_2O near the particle surface

decreases, reducing the fuel loading rate into the flame. In this limit the burn rate is therefore ultimately controlled by the rate for which AlO forms Al_2O near the particle surface, *i.e.*, a kinetically controlled process.

For burning in CO_2 and H_2O, the competition between the rate of diffusion of Al_2O from the particle surface and the rate of AlO conversion is complicated by the possibility of flame quenching. Burn time versus pressure trends for CO_2 and H_2O are shown in Figs. 3.3 and 3.4, respectively. The measurements show burn times are relatively constant for CO_2 and a slight downward trend is observed with increasing pressure for H_2O. Clearly, these cases are quite different from the O_2 runs. Earlier predictions by Washburn *et al.* (reproduced in Figs. 3.3 and 3.4) show a dramatic departure from the data, indicating increasing burn times with decreasing pressure. The current detailed model would also show trends similar to the earlier predictions of Washburn, if m_q was set to zero. Using the augmented definition of burn times that includes m_q, however, the burn times are more inline with the data showing a downward trend at lower pressures. It should be pointed out, however, that the current simulations do not yield meaningful solutions at pressures lower than $8.5atm$ for CO_2 and H_2O, where burn time measurements are reported. The reasons for these differences are potentially fourfold. The first, is the experiments employed a distribution of particles whereas the model uses a single diameter. Conceivably the emission being monitored from the experiment could therefore be from burning particles in the upper end of the distribution that are not necessarily indicative of the mean particle size. Secondly, the emission may not represent steady burning since the particles are shock ignited. In the simulations, unsteady particle burning can be achieved using an elevated initial temperature, however the particle will eventually quench due to excessive heat loss to the surroundings. Thirdly, the model currently does not include heterogeneous surface reactions since they are not available and potentially will play a role in continued burning at low pressures by introducing an adsorption catalysis via C and H atoms to increase surface energy and promote combustion reactions [40]. Fourthly, free-molecular effects of small particles have not been considered in the model and may be of importance as the kinetic limit is reached according to recent work done by Ermoline *et al.* [41]. Despite these uncertainties, changes in AlO and Al_2O near the surface in low versus high pressures shown in Figs. 3.7 and 3.8 for CO_2, and Figs. 3.9 and 3.10 for H_2O, are remarkably similar to those of O_2, highlighting the dominance of the AlO and Al_2O pathways for defining the transition from diffusion to kinetically controlled burning.

3.0.1 Consequences for Simplified Particle Modeling Descriptions

Based on detailed simulations, it is clear that effects of finite-rate chemistry must be taken into account in simplified models of aluminum particle burning. While several simplified modeling approaches have been developed for engineering estimates of particle burn times and burn rates of aluminum particles, none can account for the diffusion to kinetically controlled burning transitions. Such a model is necessary for system level simulations of multiphase flows in the

context of a subgrid scale (SGS) modeling for large eddy simulations [42, 43].

The simplest particle modeling approach are done by using burn time correlations derived using experimental data [25, 16]. Beckstead provides an excellent review on many of these prior to 2005, many taken from the Russian literature [25]. Based on a large body of data, Beckstead estimated burn times to be, $\tau_b = aD^n / X_{eff} P^{0.1} T^{0.2}$ where X_{eff} is the effective oxidizer concentration (for a mixture of O_2, H_2O and CO_2) and a, n are curve-fit constants. This correlation works well in the diffusion limited burning regimes. More recently, Lynch *et al.* [16] and Drezin *et al.* [26, 17] provided burn time corrections to account for the transitional burning regime. These correlations are very useful for when the "far-field" oxidizer, pressure and temperatures for the particle are fixed, *e.g.*, an isolated burning particle in an environment with uniform composition and temperature. For many practical applications, flows are often turbulent and therefore the far-field conditions will change throughout the particle life-time. Burn rates are therefore more useful from a modeling perspective than burn times. In the limit of diffusion controlled burning, simplified solutions for the gas-phase system can be developed using Schvab-Zeldovich coupling functions [32] or thin-flame zonal-analysis [10]. Changes in burn rates from far-field temperature, pressure and oxidizer composition can readily be computed and integrated with large-scale turbulent flow simulations [43]. These models, however, implicitly assume the mode of burning is diffusion controlled and therefore cannot account for the reduction in burn rates with decreasing particle size and pressure. As an illustration, Fig. 3.11 shows normalized burn rate "constant" (K/K_{Max}) as a function of diameter and pressures for (a) O_2, (b) CO_2 and (c) H_2O, respectively. In the limit of large particles and high pressures, K is truly a constant because the particle burns in a diffusion controlled mode, consistent with D^2 theory. $K_{max}(T, Ox)$ corresponds to the large particle/pressure limit when K is a constant and may be readily computed using simplified descriptions of the flame structure. A decrease in K/K_{max} from unity indicates particle burning transition from diffusion to kinetically controlled. In principle, these augmented $K/K_{max}(T, Ox, P, D)$ could be used with simplified D^2-type models. In this approach $K_{max}(T, Ox)$ is determined from the D^2-type model and corrected by tabulated values of K/K_{max} as a function of pressure and diameter. As an example, predictions of flame speed of aluminum dusty gases are explored over a wide range of particle sizes and pressures. Predictions are compared to the detailed simulations of Huang *et al.*[4] and experimental data of Boichuk *et al.* [5], Goroshin *et al.* [6, 7], Ballal [8] and Cassel [9] using simplified flame speed theory, $S_L = \left[-2\alpha \left(\nu + 1 \right) \overline{\dot{m}'''}_F / \rho_u \right]^{1/2}$; where α is the thermal diffusivity, ν is the mass based stoichiometric fuel to air ratio, $\overline{\dot{m}'''}_F$ is the mass consumption rate of the fuel in the mixture and ρ_u is the density of the unburned mixture [44]. Substituting in for $\overline{\dot{m}'''}_F = n_d \dot{m} = (3\rho_{air} \Phi K)/(2\nu D^2)$, where n_d is the particle density and $\dot{m}$ is the mass loss rate of the particle. The flame speed can be expressed as [45, 46]:

$$S_L = \left[\frac{3\alpha \left(\nu + 1 \right) \rho_{air}}{\rho_u} \frac{\Phi K}{\nu + \Phi} \right]^{1/2} \frac{1}{D}. \tag{3.2}$$

where Φ is the mixture equivalence ratio. In general, $K = K(T, Ox, P, D)$ but can be reexpressed as: $K = K_{max}(K/K_{max})$ where K/K_{max} comes from detailed simulations and $K_{max}(T, Ox)$ is de-

termined using the reduced model developed by DesJardin *et al.* [32] which employes Schvab-Zeldovich coupling functions to determine the gas-phase solution, assuming diffusion controlled burning. For constant values of K, Eq. (3.2) shows that S_L is inversely proportional to diameter, which is consistent with the findings of Huang *et al.* where a $D^{-0.92}$ power law was determined in the limit of large particles [4]. Decreasing particle sizes therefore results in an increase in flame speed from the associated increase in surface area. For small particles that are kinetically controlled, K deceases, resulting in a maximum in flame speed as a function of diameter. Figure 3.12 shows this behavior with comparisons of predictions using Eq. (3.2) to data [4, 5, 6, 7, 8, 9] and the limiting cases of kinetically and diffusion controlled burning modes, where S_L scales as $D^{-0.52}$ and D^{-1}, respectively. Based on experimental burn time data, Huang *et al.* derived a $D^{-0.13}$ dependence which is also included in Fig. 3.12. Good agreement is shown between model predictions, data and scaling theories considering the simplified description of flame propagation given by Eq. (3.2).

While an augmented D^2 burn rate description is useful, it requires the creation of K/K_{max} tables over a range of particle diameters and pressures. It is therefore desirable to directly incorporate the finite-rate chemistry into a reduced model. More generalized coupling functions can be defined to solve the gas-phase system which do include finite-rate chemistry and have been developed largely for coal combustion [23, 24]. While useful, these approaches are cumbersome to formulate with complex chemistry, *i.e.*, more than a single gas-phase reaction, since multiple species (more than 2) are needed to uniquely define coupling functions. Moreover, numerical integration of the energy equation is still required to obtain a solution. An alternative approach is therefore explored where Eq. (2.1) are greatly reduced by assuming: 1) gas is quasi-steady ($\dot{m} = 4\pi\rho u r^2$ is a constant), 2) equal diffusivities, 3) unity Lewis number and 4) neglecting pressure and viscous effects in momentum and energy. In this limit, transport of species and enthalpy can be expressed as:

$$\frac{\partial(\rho\beta r^2)}{\partial t} = \frac{\partial}{\partial r}\left(r^2\Gamma\frac{\partial\beta}{\partial r} - \beta\frac{\dot{m}}{4\pi}\right) + r^2\dot{S} \tag{3.3}$$

where $\beta = \{Y_i, h\}$, $\Gamma = \{\rho D_m, k/C_P\}$ and $\dot{S} = \{\dot{m}_i''', -\sum_i^N \dot{m}_i''' h_{f,i}^o\}$. This system of equations is efficiently integrated to steady-state using a fully implicit fractional step method. The result is an order of magnitude less computational effort to solve the general equations given in Eq.(2.1) since the acoustic time scales of the problem have been removed. Furthermore, based on the findings from the detailed simulations, it is clear that the dominant species governing the diffusion to kinetically controlled burning transition are Al, AlO, and Al_2O. Based on this knowledge, the original 46 reactions from the full mechanism is reduced to a set of 8 dominant reaction pathways,

$$
\begin{aligned}
Al + O_2 &\leftrightarrow AlO + O \\
Al + CO_2 &\leftrightarrow AlO + CO \\
Al + H_2O &\leftrightarrow AlO + H_2 \\
Al + AlO &\leftrightarrow Al_2O \\
2AlO + O &\leftrightarrow Al_2O_3 \\
Al_2O + 2O &\leftrightarrow Al_2O_3 \\
Al_2O_3 &\leftrightarrow Al_2O_3c \\
O_2 + M &\leftrightarrow O + O + M
\end{aligned}
$$

Figure 3.13 shows comparisons of flame structure using both approaches with full chemistry compared to solving Eq. (3.3) using the 8 step reduced mechanism for the $220\mu m$ particle burning in air shown in Fig. 3.1. All cases are compared to a baseline case using the fully compressible formulation with 50 nodes and using full chemistry. Using the simplified formulation and reaction mechanism results in an order of magnitude reduction in computational effort with little change in flame structure and an incurred 10% error in burn rates. Further savings can be introduced by reducing the number of nodes. For the 10 node case, the burn rates are still computed within a respectable $\sim$ 20% error but with nearly two orders of magnitude reduction in computational cost. Comparable trends are also observed using different oxidizers and mixtures of oxidizers (not shown).

Nodes	Speedup	Burn rate (mm^2/s)	*%error*
Baseline	1.0	0.4918	$--$
50	7.0275	0.4461	9.30
40	22.165	0.4392	10.70
30	31.706	0.4260	13.37
20	38.855	0.3922	20.26
10	72.235	0.2480	18.86

Table 3.1. Speedup comparisons using phenomenologically based reduced mechanism and quasi-steady formulation. The baseline case is fully compressible formulation using 50 nodes. All cases solved consider the burning of a 220 μm particle burning in air shown in Fig. 3.1.

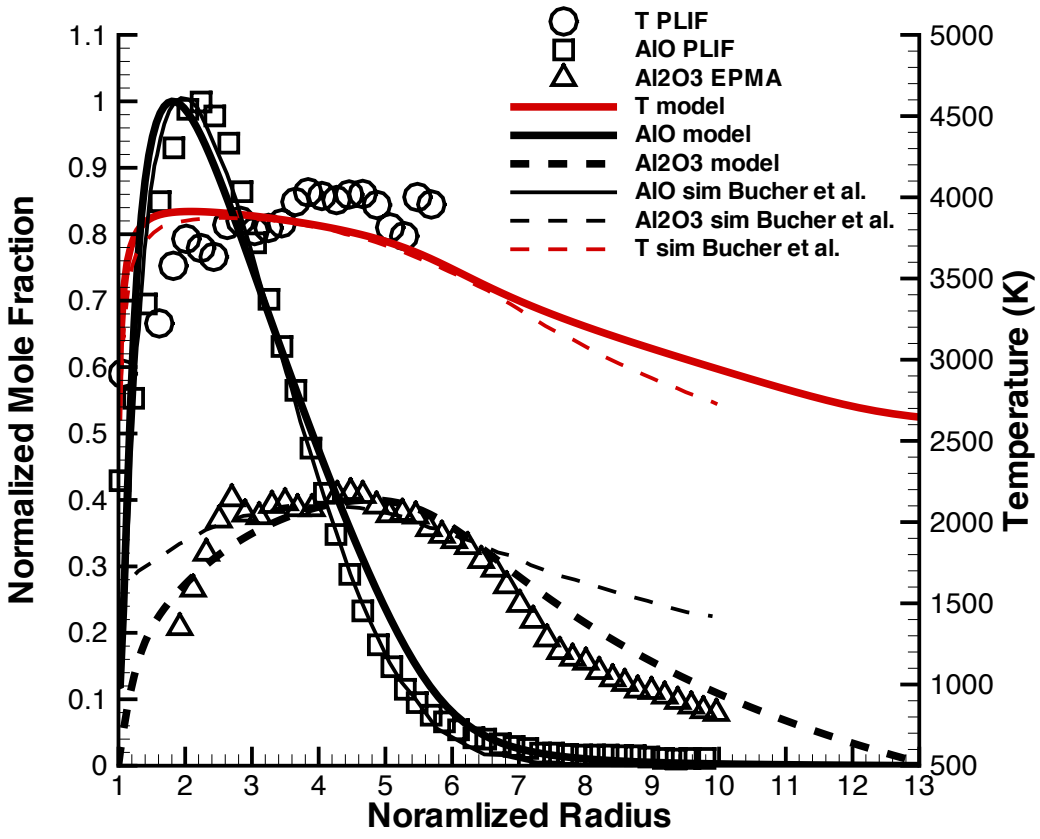

Figure 3.1. Comparisons of temperature, AlO and Al_2O_3 predictions for a 220 micron particle with atmospheric conditions $T = 2650K$, in air at $P = 1\,atm$ compared to data and simulations of Bucher *et al.* [2, 3]

.

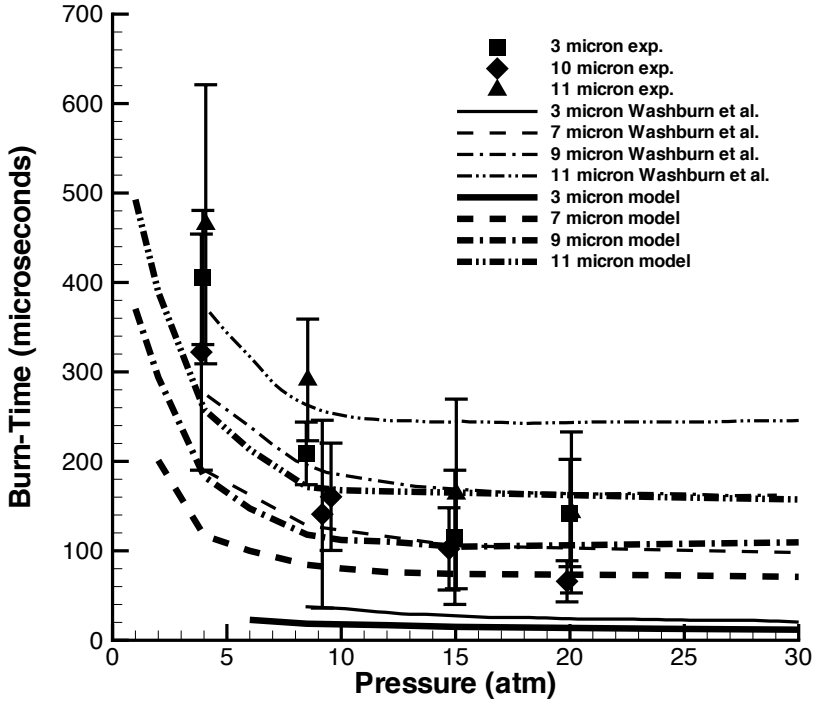

(a)

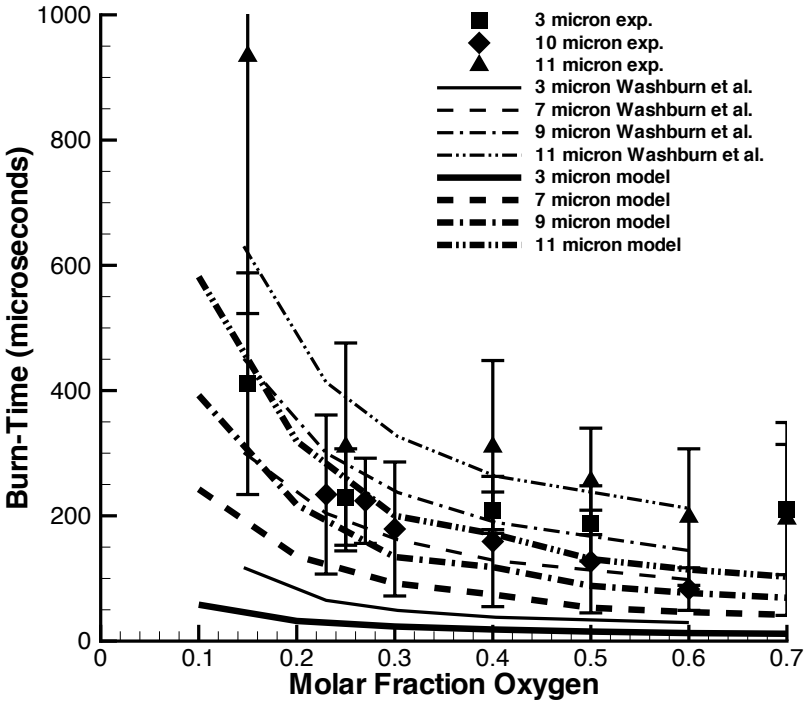

(b)

Figure 3.2. Burn time comparisons with (a) varying pressure at $T = 2650\,K$, 40% O_2 and 60% Ar and (b) varying O_2 for $P = 8.5\,atm$, $T = 2650\,K$.

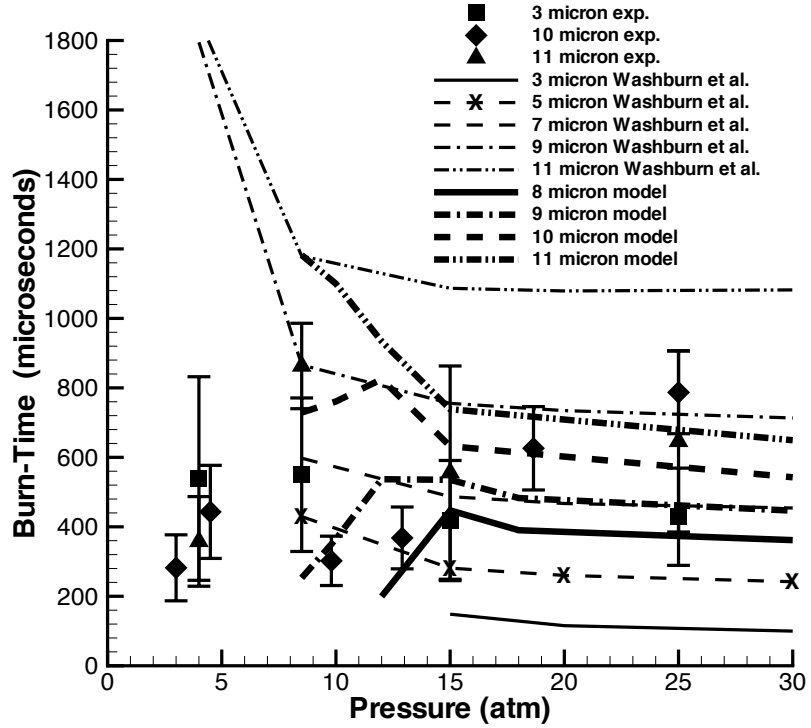

(a)

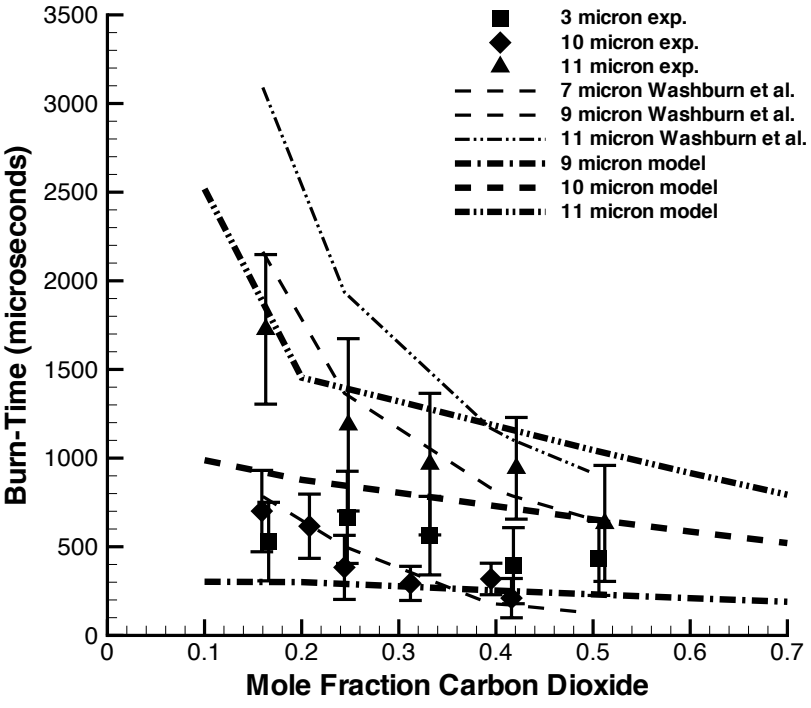

(b)

Figure 3.3. Burn time comparisons with (a) varying pressure at $T = 2650\,K$, 40% CO_2 and 60% Ar and (b) varying CO_2 for $P = 8.5\,atm$, $T = 2650\,K$.

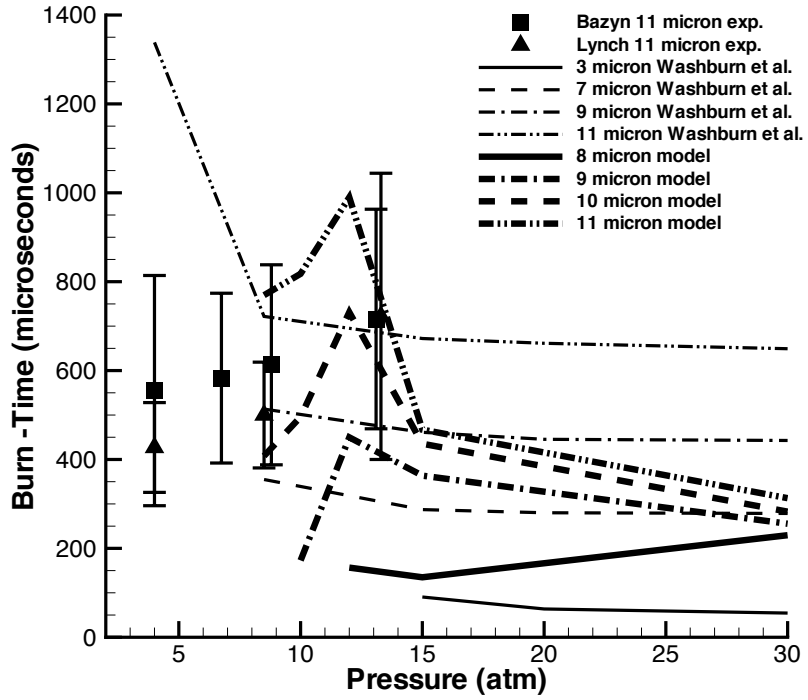

(a)

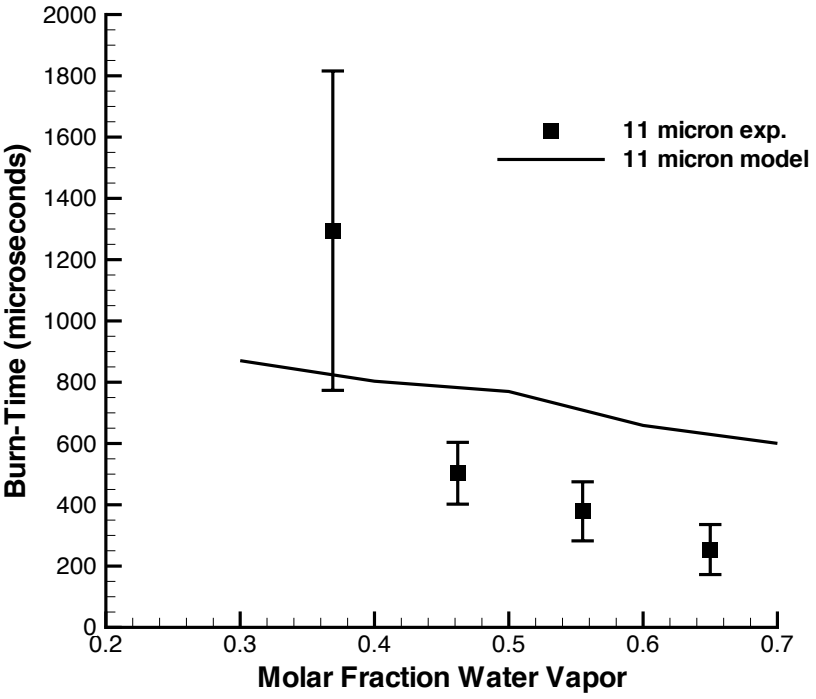

(a)

Figure 3.4. Burn time comparisons with varying pressure at $T = 2650\,K$, 50% H_2O and 50% Ar and (b) varying H_2O for $P = 8.5\,atm$, $T = 2650\,K$.

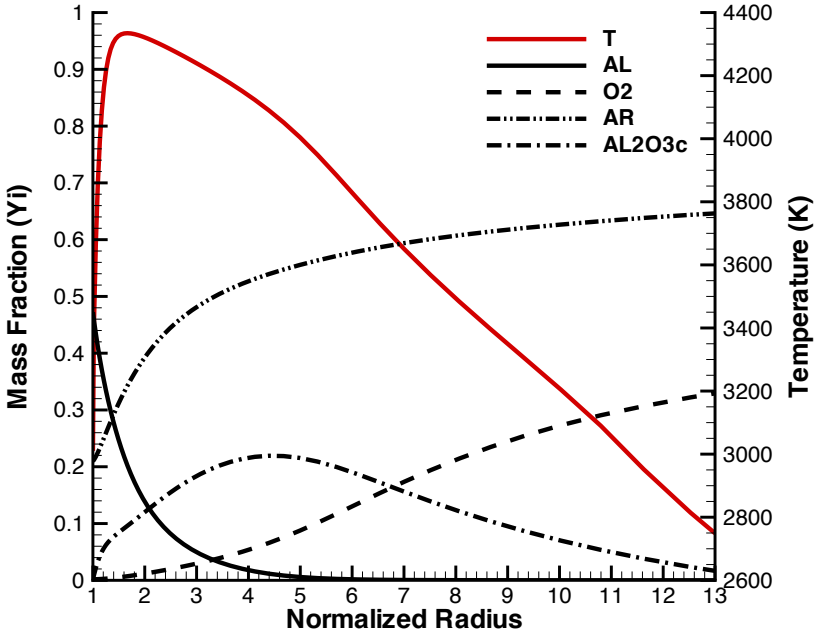

(a)

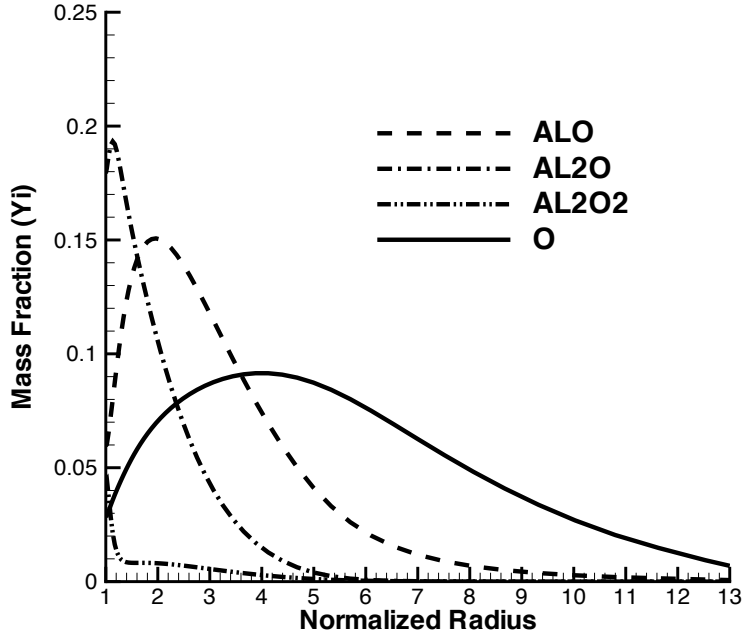

(b)

Figure 3.5. Solution as a function of normalized radius for major species and temperature (a) and minor species (b), for an 11 micron particle at atmospheric conditions $P = 4\,atm$, $T = 2650\,K$ and 40% O_2 in Ar

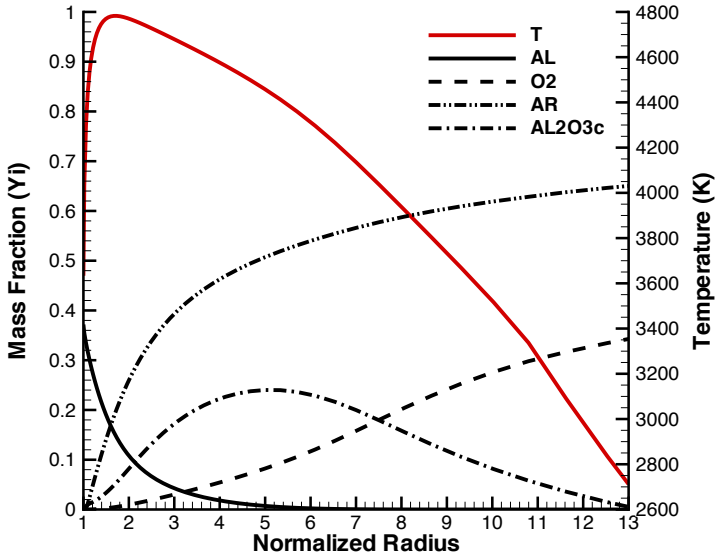

(a)

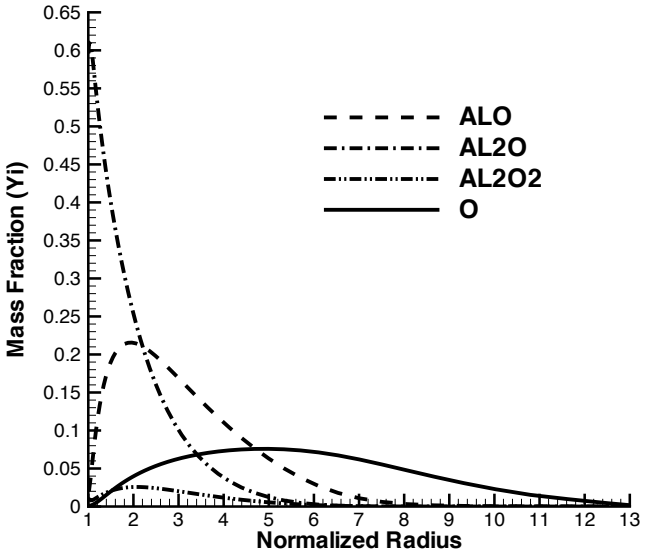

(b)

Figure 3.6. Solution as a function of normalized radius for major species and temperature (a) and minor species (b), for an 11 micron particle at atmospheric conditions $P = 30\,atm$, $T = 2650\,K$ and 40% O_2 in Ar

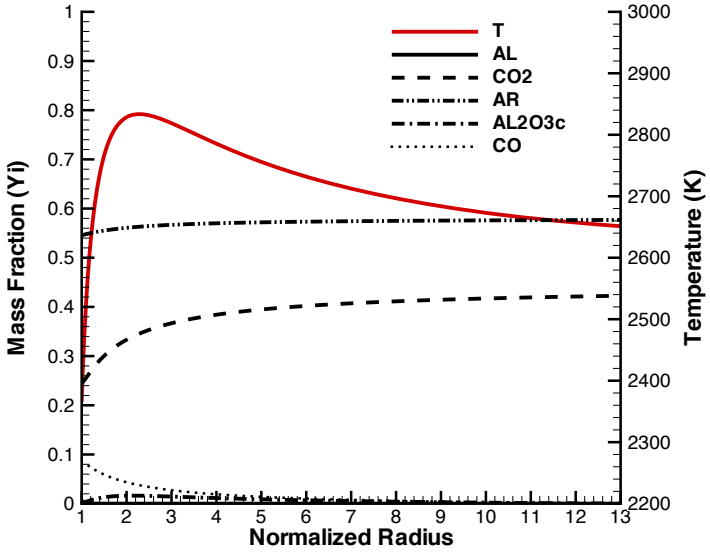

(a)

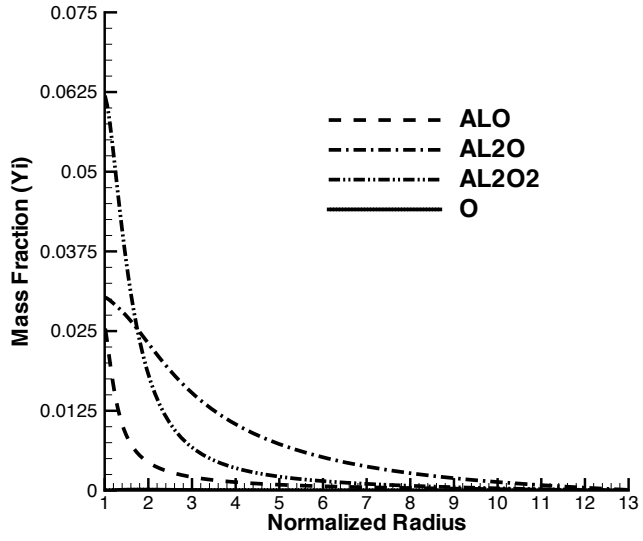

(b)

Figure 3.7. Solution as a function of normalized radius for major species and temperature (a) and minor species (b), for an 11 micron particle at atmospheric conditions $P = 10\,atm$, $T = 2650\,K$ and 40% CO_2 in Ar

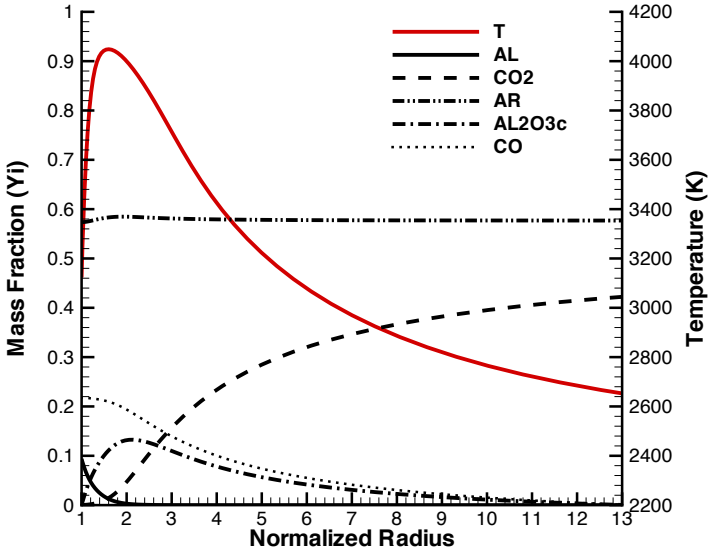

(a)

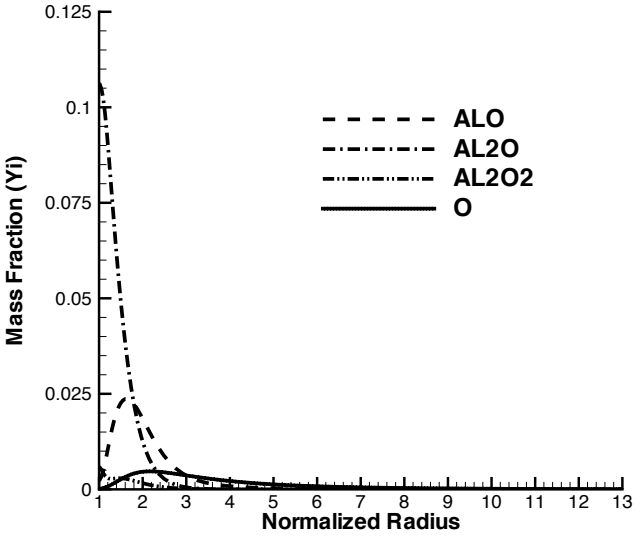

(b)

Figure 3.8. Solution as a function of normalized radius for major species and temperature (a) and minor species (b), for an 11 micron particle at atmospheric conditions $P = 30\,atm$, $T = 2650\,K$ and 40% CO_2 in Ar

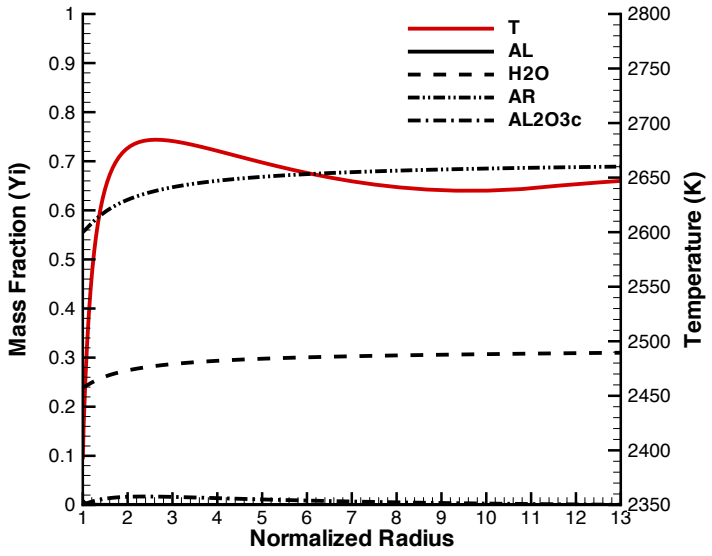

(a)

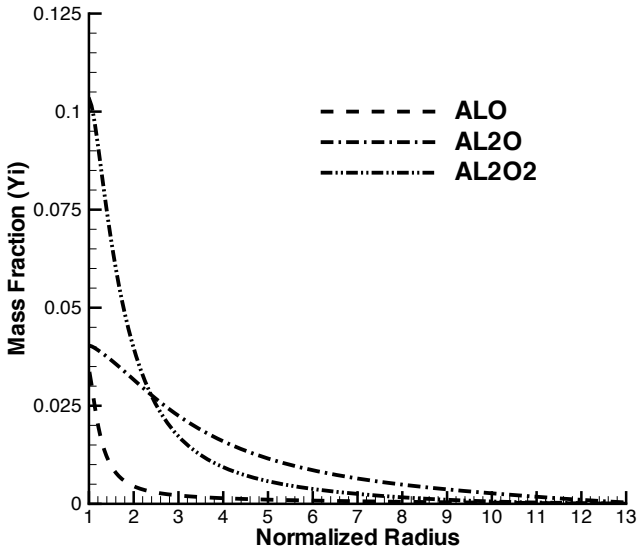

(b)

Figure 3.9. Solution as a function of normalized radius for major species and temperature (a) and minor species (b), for an 20 micron particle at atmospheric conditions $P = 12\,atm$, $T = 2650\,K$ and 50% H_2O in Ar

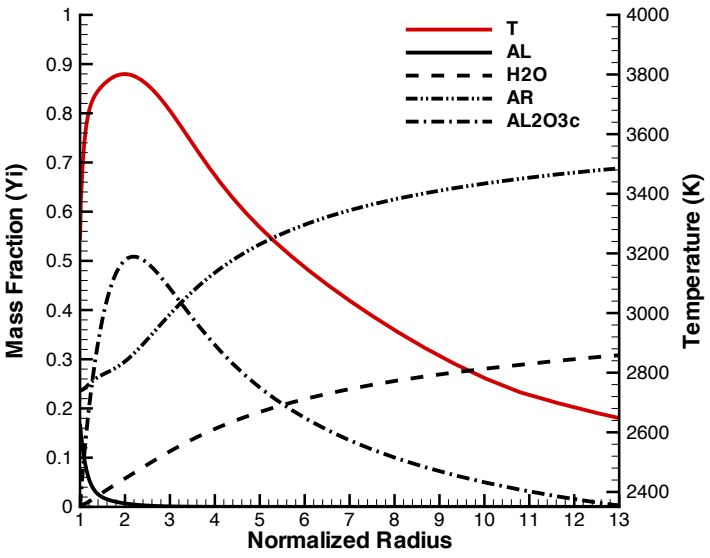

(a)

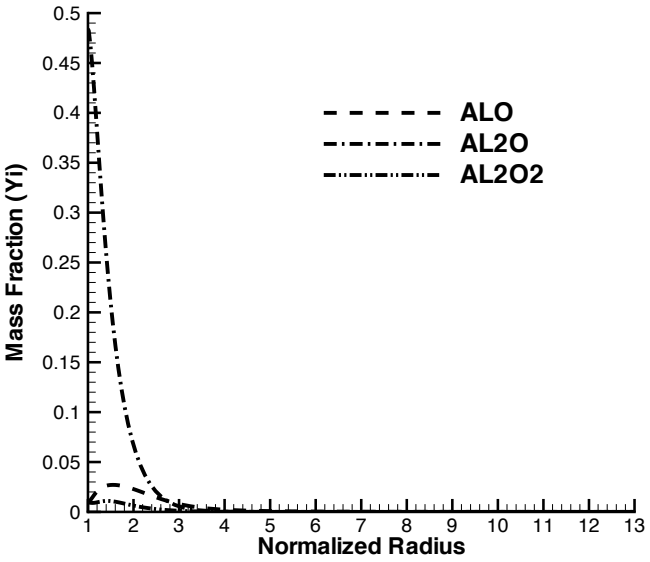

(b)

Figure 3.10. Solution as a function of normalized radius for major species and temperature (a) and minor species (b), for an 11 micron particle at atmospheric conditions $P = 30\,atm$, $T = 2650\,K$ and 50% H_2O in Ar

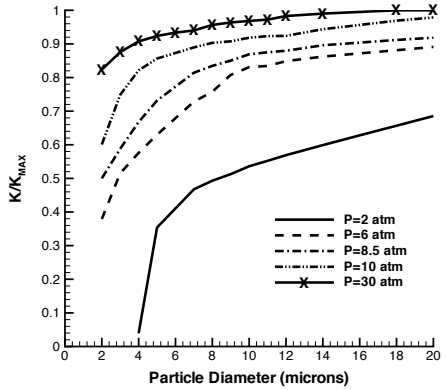

(a)

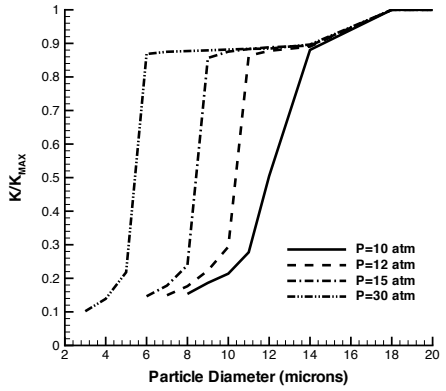

(b)

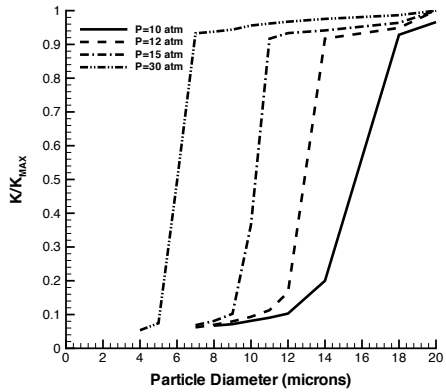

(c)

Figure 3.11. Normalized K as a function of particle diameter up to 11 microns for atmospheric conditions $T = 2650\,K$ at various pressures for (a) 40% O_2, (b) 40% CO_2 and (c) 50% H_2O.

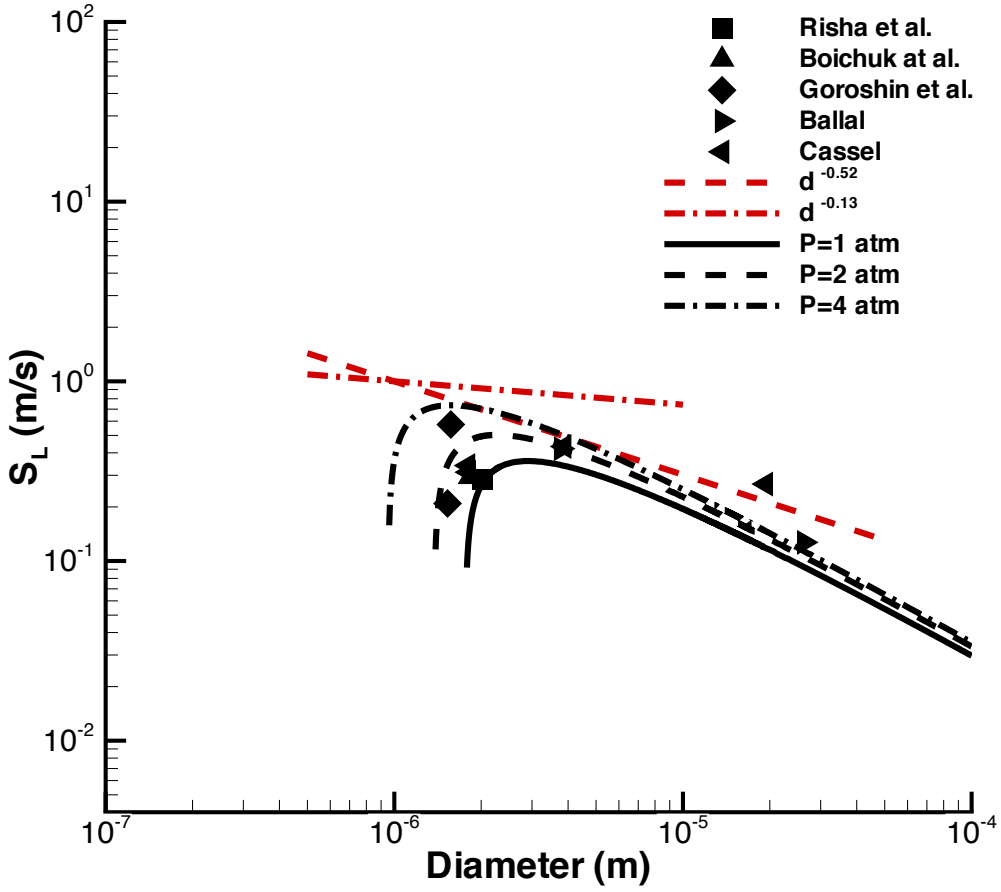

Figure 3.12. Flame speed for aluminum particles in air with, $\Phi = 0.85$, $T_\infty = 300\,K$ compared to shock tube experimental data. Experimental data from Huang *et al.* [4], Boichuk *et al.* [5], Goroshin *et al.* [6, 7], Ballal [8] and Cassel [9].

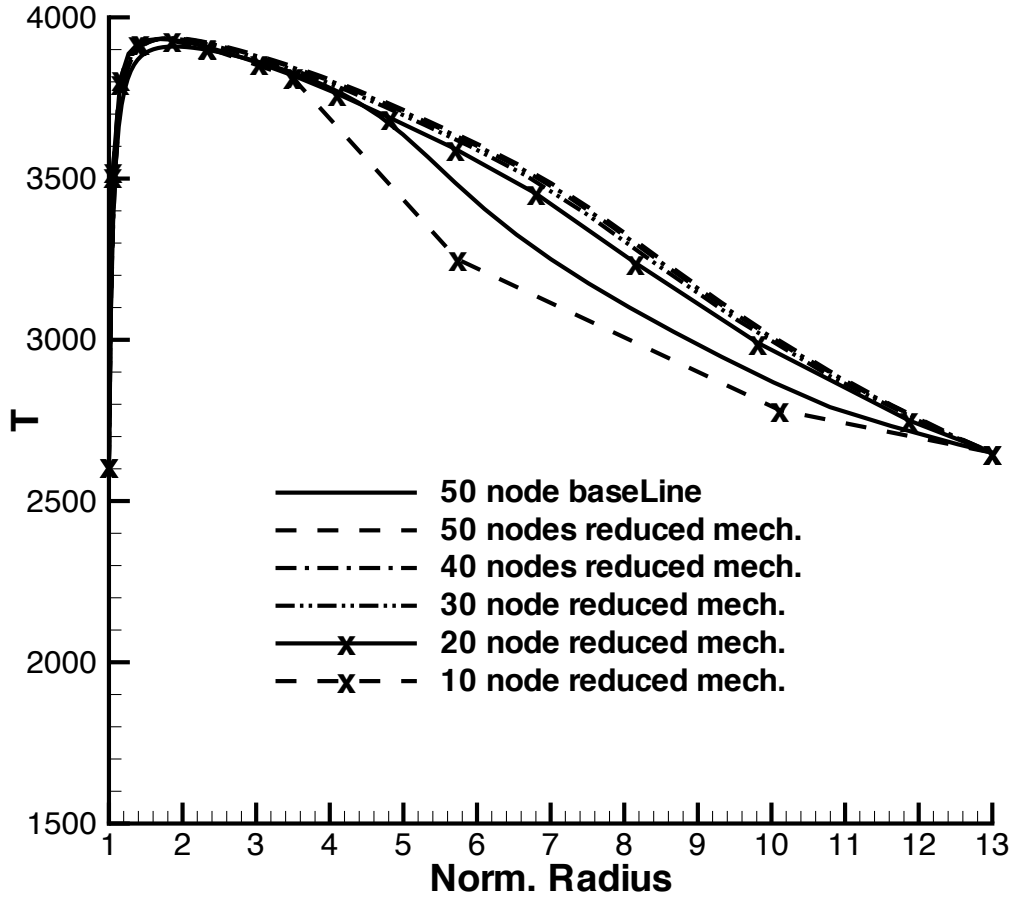

Figure 3.13. Comparisons of a reduced mechanism and number of grid points for a 220 micron particle in with atmospheric conditions $T = 2650K$, in air at $P = 1\,atm$ as previously done.

Chapter 4

Conclusion

A fully compressible, spherically symmetric aluminum particle combustion model is developed to study the transition from diffusion to kinetically controlled burning. Comparison of model predictions to multi-dimensional simulations and experimental data reveals the effectiveness of the model to reproduce the expected burn time dependencies over a range of pressures and oxidizing environments. Comparisons of the model predictions to flame structure and burn times in several different oxidizing environments compares favorably to available data. A detailed analysis of flame structure reveals the dominant pathways for the transition of diffusion to kinetically controlled burning is a competition between the consumption rate of AlO and diffusion of Al_2O away from the particle surface which is a function of both pressure and diameter. This information is used to develop two simplified modeling descriptions that can be used in system level simulations. The first is an augmented burn rate model for which the effects of finite-rate chemistry are treated as a perturbation to burn rate models assuming a thin flame structure. This approach is used to predict deflagration flame speeds of aluminum dusty gases. Agreement to data and theory is promising and shows evidence of a maximum flame speed verses diameter corresponding to a trade-off between increases in surface area and decreases in burn rates. Since the diffusion to kinetically controlled transition is largely dictated by the presence of AlO near the particle surface, it is interesting to consider means to promote AlO consumption near the surface (*e.g.*, a surface catalyst), forcing the particle to burn in a diffusion controlled mode at smaller particle sizes. If such a mechanism could be introduced, the location of maximum flame speed would potentially shift to smaller particles resulting in an overall higher peak flame speed. The second simplified modeling description relies on a reduced mechanism and a quasi-steady formulation of the equations allowing for an efficient implicit formulation. Comparisons of the reduced model compared to the fully compressible model using full kinetics shows significant savings can be achieved with little loss in accuracy for the prediction of burn rates.

Appendix A

A Mixture Fraction Approach to Numerically Model Aluminum Particle Combustion

A.1 Mixture Fraction

To better understand the rate dependent diffusion and kinetic processes, a mixture fraction based particle burn model is developed in this study. In this approach, the vapor phase equations are first recast in terms of mixture fraction space. Since the conditions at the liquid-vapor boundary interface are part of the solution, the resulting system of flamelet equations differ from those typically solved for single-phase flows (*e.g.*, an opposed-jet configuration) [47]. The appeal of this formulation is the ability to efficiently solve for the flame structure in the solution of the particle eigenvalue problem. Furthermore, analytical expressions of scalar dissipation rate allow for estimates of particle size for which burning transitions from diffusion to kinetically controlled.

A.2 Model Formulation

A spherically symmetric particle is assumed for formulating the gas phase flow. Assuming Fick's law with equal diffusivities among all species, the governing equations for species and enthalpy are given as the following set of equations,

$$\frac{1}{r^2}\frac{d}{dr}\left(\frac{\dot{m}_T}{4\pi}Y_i - \rho D r^2 \frac{dY_i}{dr}\right) = \dot{m}_i''' \tag{A.1a}$$

$$\frac{1}{r^2}\frac{d}{dr}\left(\frac{\dot{m}_T}{4\pi}h - \rho D r^2 \frac{dh}{dr}\right) = 0 \tag{A.1b}$$

where $\dot{m}_T (\equiv \dot{m}_{Al} - \dot{S}_{mox})$ is the total mass flow rate. In the derivation of Eq.(A.1b) a unity Lewis number assumption is employed and the effects of thermal radiation ignored. The boundary conditions at the liquid aluminum-gas interface are shown below as,

$$\text{Total Mass:} \qquad \dot{m}_T = \dot{m}_{Al} - \dot{S}_{mox} \tag{A.2a}$$

$$\text{Aluminum:} \qquad \dot{m}_{Al,l} = \dot{m}_T Y_{Al_s} - 4\pi r_s^2 \rho D \left.\frac{dY_{Al}}{dr}\right|_s \tag{A.2b}$$

$$\text{Aluminum Oxide:} \qquad -\dot{S}_{moxi} = \dot{m}_T Y_{moxi,s} - 4\pi r_s^2 \rho D \left.\frac{dY_{moxi}}{dr}\right|_s \tag{A.2c}$$

$$\text{All Other Species:} \qquad 0 = \dot{m}_T Y_{i,s} - 4\pi r_s^2 \rho D \left.\frac{dY_i}{dr}\right|_s \tag{A.2d}$$

$$\text{Energy:} \qquad \dot{Q}_l + \dot{m}_{Al,l} h_{Al} - \dot{S}_{moxi} h_{moxi} = \dot{m}_T h_s - 4\pi r_s^2 \rho D \left.\frac{dh}{dr}\right|_s \tag{A.2e}$$

where $\dot{S}_{moxi}$ is the rate of metal oxide deposition to the particle surface. It is assumed that condensation reaction is governed by the equilibrium between the gas and liquid phase alumina and occurs in the gas phase infinitely fast. The condensed phase alumina then migrates back to the surface of the particle to produce the alumina cap.

The quantity $\dot{Q}_l \equiv \dot{q}'' 4\pi r_s^2$ is the total heating rate of the molten aluminum. Equations (A.1) and (A.2) comprise a system of $N+1$ second order, non-linear, ordinary differential equations to solve for the eigenvalue $\dot{m}_T$ and the thermodynamic state at the vapor surface. The total number of unknowns includes the composition and enthalpy at the surface $(N+1)$, the mass flow rates of inert and oxidizer in the liquid along with the metal oxide deposition rates $(N+1)$ and the heating of liquid for a total of $2(N+1)$ unknowns. Given that the far-field conditions are known, $N+1$ constraints are required to close the system which are defined by either specifying the flow rate of mass or energy into the liquid phase or specifying values at the surface. Assuming steady-state burning and insolubility of the oxidizer and inert species in the molten aluminum then $\dot{Q}_l = \dot{m}_{ox,l} = \dot{m}_{I,l} = 0$. The deposition of metal oxide is assumed to be sufficiently fast that the mass fraction of the alumina species is zero at the surface. This assumption provides an upper limit on the amount of metal oxide that can be deposited to the surface - similar to previous studies [32].

For the limiting case of infinitely fast chemistry and a single metal oxide product, these equations can be reduced to a system of non-linear algebraic equations and solved via coupling functions [32]. Including detailed chemistry requires a numerical solution which can be efficiently solved by recasting Eqs.(A.1) and (A.2) in terms of a mixture fraction coordinate, $Z = Y_{Al} + \sum \nu_{mox,i} Y_{Al_n O_m}$ where $\nu_{mox,i} (\equiv nMW_{Al}/MW_{Al_n O_m})$ is the mass ratio of aluminum to total mass of the oxide. Since Z is a conserved scalar, its transport equation is identical to that of Eq. (A.1b) with h replaced with Z. Integrating this expression and using the boundary condition at the droplet surface: $\dot{m}_{Al} - \nu_{moxi} \dot{S}_{moxi} = \dot{m}_Z = \dot{m}_T Z_s - 4\pi\rho D r_s^2 dZ/dr|_s$ then the derivative of Z at the droplet surface can be expressed as: $dZ/dr|_s = \left(\dot{m}_T Z_s - \dot{m}_Z\right) / \left(4\pi\rho D r_s^2\right)$, where $\dot{m}_Z$ is the total mass flow rate mixture fraction. Using this result, the boundary conditions for the

species given in Eq. (A.2) can be remapped into the following augmented system.

$$\text{Aluminum: } \dot{m}_{Al,l} = \dot{m}_T Z_s - (\dot{m}_T Z_s - \dot{m}_Z) \left.\frac{dY_{Al}}{dZ}\right|_s \tag{A.3a}$$

$$\text{Aluminum Oxide Species: } -\dot{S}_{mox} = Y_{mox}|_s \dot{m}_T - (\dot{m}_T Z_s - \dot{m}_Z) \left.\frac{dY_{mox}}{dZ}\right|_s \tag{A.3b}$$

$$\text{All Other Species: } 0 = Y_i|_s \dot{m}_T - (\dot{m}_T Z_s - \dot{m}_Z) \left.\frac{dY_i}{dZ}\right|_s \tag{A.3c}$$

Due to the nature of metallic combustion where the final oxidized metal product is in a condensed form, combustion temperatures are limited by the volatilization temperature of the metal oxide [48]. The surface boundary condition for the energy equation in terms of temperature in mixture fraction space is shown in Eq. (A.5), where h_{lg} is the latent heat of vaporization of aluminum and c_p is the specific heat at constant pressure.

$$\frac{\rho\chi}{2}\frac{d^2T}{dZ^2} = \frac{\sum \dot{m}_i''' \Delta h^o_{f,i}}{c_p} \tag{A.4}$$

$$\dot{m}_{Al,l} h_{lg} = c_p \left(\dot{m}_T Z_s - \dot{m}_z\right) \frac{dT}{dZ}|_s \tag{A.5}$$

Transforming the steady-state species transport equations results in a second-order non-linear ODE for each species, also know as the flamelet equation:

$$\frac{d^2Y_i}{dZ^2} = \frac{2}{\rho\chi}\dot{m}_i''' \tag{A.6}$$

where $\chi\ (\equiv \rho D|\nabla Z|^2)$ is the scalar dissipation rate that is determined directly from the solution of the Z transport equation (which is the same as Eq. (A.1b) with h replaced by Z) leading to the result,

$$\chi = 2D\left(\frac{\dot{m}_T Z - \dot{m}_z}{4\pi\rho D r^2}\right)^2. \tag{A.7}$$

Near the flame at $Z = Z_{st}$, χ_{st} is proportional to $1/r^4$, indicating that the loading of the flame will be a strong function of particle size. As the particle radius decreases, χ increases rapidly, reducing the effective chemical rates *via* Eq. (A.6). A reduction in the conversion rates results in the transition of burning from diffusion to kinetics controlled. Based on these analytics, it is reasonable to assume that all burning droplets will transition from diffusion to kinetics controlled modes of burning. The importance of the kinetically controlled burning regime of a droplet is therefore a function of what fraction the total burning time is dominated by kinetic effects. Figure A.1 shows predictions of χ_{st} using the theory with comparisons to the detailed simulations of Washburn *et al.* [30, 14] for the burning of *Al* particles in air. The overall agreement is reasonable and shows a $1/r^4$ dependence as $r \to 0$. Based on experimental data, Badiola, Gill and Dreizen observe that Al particle burning transition at for 7.4 μm particles [49]. According to Fig. A.1, the corresponding value of χ_{st} is approximately $5 * 10^5$ (1/s) which is nearly 5,000

times larger than quenching values (χ_q) often cited for counter-flow laminar diffusion flames [47]. The differences arising from the fact that the mass flux is conserved for counter-flow diffusion flames while the overall mass flow rate is conserved for burning particle. In addition, the boundary conditions for the spherical particle given in Eq. (A.3) are different than those for counter-flow flames.

Using surface boundary conditions for Z and h in Eq.(A.2e) and the far-field conditions that is, as $r \to \infty$, $Z \to Z_\infty$ and $h \to h_\infty$ then the solutions for Z and h are the following,

$$\dot{m}_T = 4\pi r \rho D \, ln \left(\frac{\dot{m}_Z Z_\infty - \dot{m}_T}{\dot{m}_Z Z - \dot{m}_T} \right) \tag{A.8a}$$

$$\dot{m}_T = 4\pi r \rho D \, ln \left(\frac{\dot{q}_z' h_\infty - 1}{\dot{q}_z' h - 1} \right) \tag{A.8b}$$

where $\dot{m}_Z' = \dot{m}_T / \dot{m}_Z$ and $\dot{q}' = \dot{m}_T / \dot{q}_z$. Equating these expressions, then h can be directly expressed in terms of Z, $h = (1/\dot{q_z}') \left[(\dot{q_z}' h_\infty - 1) \left(1 - \dot{m_z}' Z \right) + 1 \right]$.

With an initial guess of Z_s, $\dot{m}_T$ and $\dot{m}_Z$ are initialized using the boundary conditions with gradients estimated from an infinitely fast chemistry assumption. The flamelet equations given in Eq. (A.6) are then solved using a transient solution method. After the steady-solution of the flamelet equations are obtained, $\dot{m}_z'$ and $\dot{q}_z'$ are updated using the following relations,

$$\dot{m}_z' = \frac{1 - \dot{S}_{mox}'}{1 - \dot{S}_\nu \dot{S}_{mox}'} \tag{A.9a}$$

$$\dot{q}_z' = \frac{\dot{m}_T}{\dot{m}_{Al,l} h_{Al} - \dot{S}_{moxi} h_{moxi}} \tag{A.9b}$$

$$\dot{S}_{mox}' = \frac{\dot{S}_{mox}}{\dot{m}_{Al}} = \left[\frac{(1 - Z_s) \left(1 - \frac{dY_{Al}}{dZ}|_s \right)}{Z_s \left(\frac{dY_{Al}}{dZ}|_s - 1 \right) - \dot{S}_\nu \frac{dY_{Al}}{dZ}|_s} \right] \tag{A.9c}$$

$$\dot{S}_\nu = \frac{\nu_{Al_2O_3} \frac{dY_{Al_2O_3}}{dZ}|_s}{\frac{dY_{Al_2O_3}}{dZ}|_s} = \nu_{Al_2O_3} \tag{A.9d}$$

where $\dot{S}_\nu$ represents the fraction of oxide deposited to the surface that has a contribution to the overall mixture fraction. $\dot{S}_{mox}'$ is the ratio of oxide deposition to vapor mass flow rates. In the limit of no deposition, $\dot{S}_{mox}' \to 0$ then $\dot{m}_z' \to 1$ and $\dot{q}_z' \to 1/h_{Al,l}$ where $h_{Al,l}$ is the liquid aluminum enthalpy.

The mass flux of Al from the surface and the deposition of the Al oxide can be determined when the eigenvalue solver is converged and particle burn times can be calculated via mass integration over the initial mass with a variable mass loss rate of aluminum, $t_b = \int_0^{m_o} \frac{1}{\dot{m}_{Al}} dm$. It has been confirmed from the data such burn times are in fact equivalent to a D^2 law and the error between the mass integration, where the error decreases as the particle size increases. A geometrical consideration of cap formation was considered by assuming the alumina cap and

liquid aluminum intersected as two spheres. However, when calculating burn times with a mass integration considering variable solid angle, evaporation and deposition rates, burn times were found to increase by $\sim$ 15% compared with burn times without a shape factor considered. To reduce the computational cost of integrating from initial particle size to burnout, the burn-times can be sufficiently calculated by using the D^2 law, where the burn constants K, are defined as $K = 4\dot{m}_{Al}/(\pi\rho_{Al}D_p)$. Although a variable burn constant is now introduced, it is advantageous because computational time is significantly decreased with a steady state burn assumption as compared to a time integrated method.

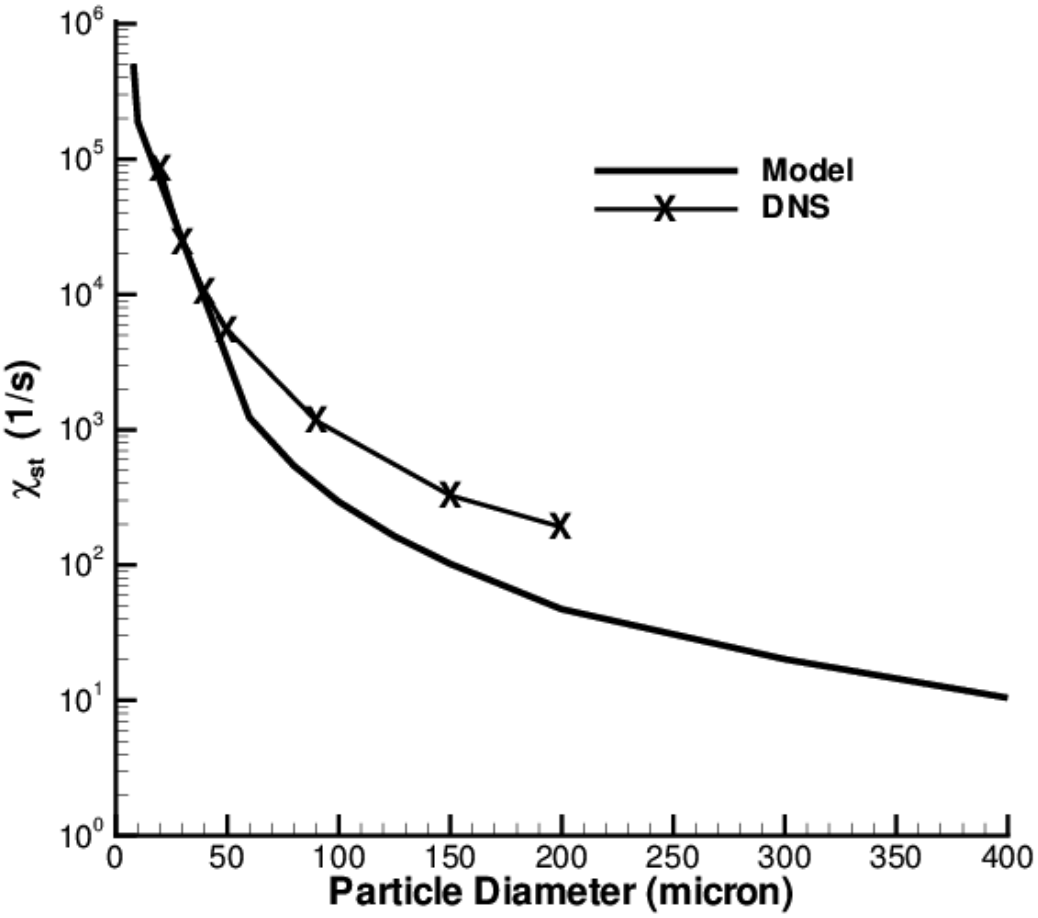

Figure A.1. Scalar dissipation rate, χ, as a function of particle diameter in air, $P = 1\,atm$, $T = 2650\,K$

Appendix B

Aluminum Combustion Mechanism

Kinetic mechanism for aluminum combustion with air, steam and carbon dioxide.

Reaction	$A\ [cm^3/mol/s]$	α	E_a (K)
$Al + O_2 \leftrightarrow AlO + O$	9.72×10^{13}	0.0	80.5
$AlO + O_2 \leftrightarrow AlO_2 + O$	4.62×10^{14}	0.0	10008.0
$Al_2O_3 \leftrightarrow Al_2O_3c$	3.0×10^{15}	0.0	0.0
$Al_2O_3 \leftrightarrow Al_2O_2 + O$	3.0×10^{15}	0.0	49144.4
$Al_2O_3 \leftrightarrow AlO_2 + AlO$	3.0×10^{15}	0.0	63915.1
$Al_2O_2 \leftrightarrow Al + AlO_2$	1.0×10^{15}	0.0	74937.1
$Al_2O_2 \leftrightarrow AlO + AlO$	1.0×10^{15}	0.0	59335.7
$Al_2O_2 \leftrightarrow Al_2O + O$	1.0×10^{15}	0.0	52466.0
$AlO_2 \leftrightarrow AlO + O$	1.0×10^{15}	0.0	44564.6
$Al_2O \leftrightarrow AlO + Al$	1.0×10^{15}	0.0	67035.7
$Al + O + M \leftrightarrow AlO + M$ $H_2/2.8/O_2/1.1/H_2O/1.1/$ $CO_2/4.3/CO/2.1/$	3.0×10^{17}	-1.0	0.0
$O_2 + M \leftrightarrow O + O + M$	1.2×10^{14}	0.0	54244.0
$Al + H_2O \leftrightarrow H + AlOH$	1.14×10^{12}	0.0	442.88
$Al + H_2O \leftrightarrow AlO + H_2$	9.6×10^{13}	0.0	2868.64
$H_2 + M \leftrightarrow H + H + M$	2.23×10^{14}	0.0	48350.0
$AlH_3 + H \leftrightarrow AlH_2 + H_2$	4.75×10^{9}	1.5	0.0
$AlH_3(+M) \leftrightarrow AlH + H_2(+M)$ $LOW/1.01 \times 10^{15}\ 0.0\ 27089.0/$ $TROE/0.06\ 885.0\ 552.0\ 3807.0/$	1.48×10^{13}	0.0	30758.9
$Al + H + M \leftrightarrow AlH + M$	1.6×10^{17}	-0.34	0.0
$AlH + H \leftrightarrow Al + H2$	1.0×10^{13}	0.0	0.0
$AlH_2 + H \leftrightarrow AlH + H_2$	2.0×10^{13}	0.0	0.0
$AlH_2(+M) \leftrightarrow AlH + H(+M)$ $LOW/9.68 \times 10^{14}\ 0.0\ 19962.0/$ $TROE/5.1\ 21.6\ 493.0\ 942.0/$	2.23×10^{14}	0.0	48350.0

Reaction	$A\ [cm^3/mol/s]$	α	E_a (K)
$Al + CO_2 \leftrightarrow AlO + CO$	1.74×10^{14}	0.0	3221.4
$AlO + CO_2 \leftrightarrow AlO_2 + CO$	1.5×10^{10}	0.0	-400.1
$H + O + M \leftrightarrow OH + M$	6.2×10^{16}	-0.6	0.0
$H + O_2 \leftrightarrow OH + O$	1.59×10^{17}	-0.927	8492.7
$H_2 + O \leftrightarrow OH + H$	3.87×10^{4}	2.7	3151.8
$H_2 + OH \leftrightarrow H_2O + H$	2.16×10^{8}	1.51	1732.3
$OH + OH \leftrightarrow H_2O+)$	2.10×10^{8}	1.4	-199.7
$H + O_2 + M \leftrightarrow HO_2 + M$	7.0×10^{17}	-0.8	0.0
$HO_2 + H \leftrightarrow OH + OH$	1.5×10^{14}	0.0	505.2
$HO_2 + H \leftrightarrow H_2 + O_2$	2.5×10^{13}	0.0	348.8
$HO_2 + H \leftrightarrow H_2O + O$	5.0×10^{12}	0.0	709.6
$HO_2 + O \leftrightarrow O_2 + OH$	2.0×10^{13}	0.0	0.0
$HO_2 + OH \leftrightarrow H_2O + O_2$	6.02×10^{13}	0.0	0.0
$HO_2 + HO_2 \leftrightarrow H_2O_2 + O_2$	4.2×10^{14}	0.0	6030.7
$H_2O_2 + H \leftrightarrow HO_2 + H_2$	1.7×10^{12}	0.0	1888.7
$H_2O_2 + H \leftrightarrow H_2O + OH$	1.0×10^{13}	0.0	1804.4
$H_2O_2 + O \leftrightarrow HO_2 + OH$	2.8×10^{13}	0.0	3223.9
$H_2O_2 + OH \leftrightarrow H_2O + HO_2$	7.0×10^{12}	0.0	721.7
$AlOH \leftrightarrow AlO + H$	1.0×10^{15}	0.0	57731.2
$AlOH \leftrightarrow Al + OH$	1.0×10^{15}	0.0	66438.3
$H + OH + M \leftrightarrow H_2O + M$ $H_2/1.9/O_2/2.6/H_2O/9.5/$ $CO/2.6/CO_2/2.6/$	8.4×10^{21}	-2.0	0.0
$H_2O_2 + M \leftrightarrow OH + OH + M$ $H_2/2.9/O_2/1.2/H_2O/18.5/$ $CO/2.1/CO_2/4.3/$	1.0×10^{17}	0.0	22856.4
$CO_2(+M) \leftrightarrow CO + O(+M)$ $LOW/5.1 \times 10^{14}\ \ 0.0\ \ 55561.0/$	9.0×10^{12}	0.0	65280.3
$CO + O_2 \leftrightarrow CO_2 + O$	2.53×10^{12}	0.0	24003.5
$CO + OH(+M) \leftrightarrow CO_2 + H(+M)$ $LOW/1.17 \times 10^{7}\ \ 1.35\ \ -360.8/$	2.45×10^{-3}	3.68	-625.5
$CO + HO_2 \leftrightarrow CO_2 + OH$	6.40×10^{9}	0.0	11873.3

Bibliography

[1] I. Glassman. *Combustion*. Academic Press, New York, NY, 1996.

[2] P. Bucher, R. A. Yetter, F. L. Dryer, T. P. Parr, D. M. Hanson-Parr, and E. P. Vicenzi. Flame structure measurement of single, isolated aluminum particles burning in air, 1996.

[3] P. Bucher, R. A. Yetter, F. L. Dryer, E. P. Vicenzi, T. P. Parr, and D. M. Hanson-Parr. Condensed-phase species distributions about al particles reacting in various oxidizers. *Combust. Flame*, 117:351–361, 1999.

[4] Ying Huang, Grant A. Risha, Vigor Yang, and Richard A. Yetter. Effect of particle size on combustion of aluminum particle dust in air. *Combustion and Flame*, 156(1):5–13, 1 2009.

[5] L. V. Boichuk, V. G. Shevchuk, and A. I. Shvets. Flame propagation in two-component aluminumboron gas suspensions. *Combustion, Explosion, & Shock Waves*, 38(6):651–654, 11 2002.

[6] S. Goroshin, I. Fomenko, and J. H. S. Lee. Burning velocities in fuel-rich aluminum dust clouds. *Symposium (International) on Combustion*, 26(2):1961–1967, 1996.

[7] S Goroshin, M Bidabadi, and J. H. S Lee. Quenching distance of laminar flame in aluminum dust clouds. *Combustion and Flame*, 105(1–2):147–160, 4 1996.

[8] D. R. Ballal. Flame propagation through dust clouds of carbon, coal, aluminium and magnesium in an environment of zero gravity. *Proceedings of the Royal Society of London. Series A, Mathematical and Physical Sciences*, 385(1788):21–51, 01 1983.

[9] H.M. Cassel. Reports of investigations 6551. *U. S. Dept. Interior Bureau of Mines*, 1963.

[10] M. K. King. Aluminum combustion in a solid rocket motor environment. *Proc. Combust. Inst.*, 32:2107–2114, 2009.

[11] S. R. Turns, S. C. Wong, and E. Ryba. Combustion of aluminum-based slurry agglomerates. *Combust. Sci and Tech.*, 54:299–318, 1987.

[12] Yanan Gan and Li Qiao. Combustion characteristics of fuel droplets with addition of nano and micron-sized aluminum particles. *Combustion and Flame*, 158(2):354–368, 2 2011.

[13] T. Bazyn, H. Krier, and N. Glumac. Evidence for the transition from the diffusion-limit in aluminum particle combustion. *Proc. Combust. Inst.*, 31:2021–2028, 2007.

[14] E. B. Washburn, J. A. Webb, and M. W. Beckstead. The simulation of the combustion of micrometer-sized aluminum particles with oxygen and carbon dioxide. *Comb. and Flame*, 157:540–545, 2010.

[15] Salil Mohan, Luc Furet, and Edward L. Dreizin. Aluminum particle ignition in different oxidizing environments. *Combustion and Flame*, 157(7):1356–1363, 7 2010.

[16] Patrick Lynch, Herman Krier, and Nick Glumac. A correlation for burn time of aluminum particles in the transition regime. *Proceedings of the Combustion Institute*, 32(2):1887–1893, 2009.

[17] C. Badiola, R. J. Gill, and E. L. Dreizin. Combustion characteristics of micron-sized aluminum particles in oxygenated environments. *Combustion and Flame*, 158(10):2064–2070, 10 2011.

[18] E. B. Washburn, J. N. Trivedi, L. Catoire, and M.W. Beckstead. The simulation of the combustion of micrometer-sized aluminum particles with steam. *Combustion Science and Technology*, 108:8:1502–1517, 2008.

[19] T. Bazyn, H. Krier, and N. Glumac. Oxidizer and pressure effects on the combustion of 10-micron aluminum particles. *J. Propulsion and Power*, 21:577–582, 2005.

[20] M. W. Beckstead. A summary of aluminum combustion. Rto, 1995.

[21] Laurent Catoire, Jean-Fran-atilde, ois Legendre, and Marc Giraud. Kinetic model for aluminum-sensitized ram accelerator combustion. *Journal of Propulsion and Power*, 19(2):196–202, 2013/02/25 2003.

[22] R. A. Yetter and F.L. Dryer. *Microgravity Combustion: Fire in Free Fall*. pp. 419-478. Academic Press, 2001.

[23] A. Makino and C. K. Law. Quasi-steady and tranient combustion of a carbon particle: Theory and experimental comparisons. In *Twenty-first Symposium (Int.) on Combustion*, pages 183–191. The Combustion Institute, 1986.

[24] A. Makino. An approximate explicit expression for the combustion rate of a small carbon particle. *Combust. and Flame*, 90:143–154, 1992.

[25] M.W. Beckstead. Correlating aluminum burning times. *Combustion, Explosion, & Shock Waves*, 41(5):533–546, 2005.

[26] R. J. Gill, C. Badiola, and E. L. Dreizin. Combustion times and emission profiles of micron-size aluminum particles burning in different environments. *Comb. and Flame*, 157:2015–2023, 2010.

[27] S. Gallier, F. Sibe, and O. Orlandi. Combustion response of an aluminum droplet burning in air. *Proc. Combust. Inst.*, 33:1949–1956, 2011.

[28] S. Mathur, P.K. Tondon, and S.C. Saxena. Thermal conductivity of binary, ternary and quaternary mixtures of rare gases. *Molecular Physics*, 12:569, 1967.

[29] R.B. Bird, W.E. Stewart, and E.N. Lightfoot. *Transport Phenomena*. John Wiley and Sons, 1960.

[30] L. Wullschleger and K. G. Wakili. Numerical parameter study of the thermal behavior of a gypsum plaster board at fire temperatures. *Fire and Materials*, 32:103–119, 2008.

[31] Alexander M. Starik, Pavel S. Kuleshov, Alexander S. Sharipov, Nataliya S. Titova, and Chuen-Jinn Tsai. Numerical analysis of nanoaluminum combustion in steam. *Combustion and Flame*, (0):–, 2013.

[32] P.E. DesJardin, J. D. Felske, and M. D. Carrara. Mechanistic model of aluminum particle ignitiona and combustion in air. *J. Propulsion and Power*, 21(1):1–8, 2005.

[33] V. A. Babuk and V.A. Vasilyev. Model of aluminum agglomerate evolution in combustion products of solid rocket propellant. *J. Propulsion and Power*, 18(4):814–823, 2002.

[34] R. Hultgren, P. D. Desai, D. T. Hawkins, M. Gleiser, and K. K. Kelley. *Selected Values of the Thermodynamics Properties of the Elements*. Americal Society for Metals, 1973.

[35] Meng-Sing Liou. A sequel to ausm, part ii: Ausm+up for all speeds. *J. Comp. Physics*, 214(1):137 – 70, 2006.

[36] Y. Li. Wavenumber-extended high-order upwind-biased finite-difference schemes for convective scalar transport. *J. Comput. Phys.*, 133:235–255, 1997.

[37] J. A. Sethian and S. J. Osher. The design of algorithms for hypersurfaces moving with curvature-dependent speed, 1989. Notes on Numerical Fluid Mechanics, Volume 24.

[38] Mark T. Swihart and Laurent Catoire. Thermochemistry of aluminum species for combustion modeling from ab initio molecular orbital calculations. *Combustion and Flame*, 121(1–2):210–222, 4 2000.

[39] P. Lynch, H. Krier, and N. Glumac. Micro-alumina particle volatilization temperature measurements in a heterogenous shock tube. *Combustion and Flame*, 159:793–801, 2012.

[40] V. Sarou-Kanian, J.C. Rifflet, F. Millot, and I. Gökalp. Aluminum combustion in wet and dry co2: Consequences for surface reactions. *Combustion and Flame*, 145(1–2):220 – 230, 2006.

[41] Alexandre Ermoline, Deniz Yildiz, and Edward L. Dreizin. Model of heterogeneous combustion of small particles. *Combustion and Flame*, 160(12):2982 – 2989, 2013.

[42] K. P. Ruggirello, P.E. DesJardin, M. R. Baer, and E. S. Hertel. Modeling of particle compressibility and ignition from shock-shock focusing. *Combust. Theory Modelling*, 14:41–67, 2010.

[43] K. P. Ruggirello, P. E. DesJardin, M. R. Baer, M. J. Kaneshige, and E. S. Hertel. A reaction progress variable modeling approach for non-ideal multiphase explosives. *International Journal of Multiphase Flow*, 42(0):128–151, 6 2012.

[44] S. R. Turns. *An Introduction to Combustion*. McGraw-Hill, Inc., New York, NY, 1996.

[45] F. A. Williams. *Combustion Theory*. The Benjamin/Cummings Publishing Company, Menlo Park, CA, 1985.

[46] C. K. Law. *Combustion Physics*. Cambridge University Press, 2006.

[47] N. Peters. *Turbulent Combustion*. Cambridge University Press, Cambridge, UK, 2000.

[48] I. Glassman and R. A. Yetter. *Combustion*. Academic Press, 2008.

[49] Carlo Badiola, Robert J. Gill, and Edward L. Dreizin. Combustion characteristics of micron-sized aluminum particles in oxygenated environments. *Combustion and Flame*, 158(10):2064–2070, 10 2011.